IS-T 1728

Development of a new Pb-free solder: Sn-Ag-Cu

by

Miller, Chad M.

MS Thesis submitted to Iowa State University

Ames Laboratory, U.S. DOE
Iowa State University
Ames, Iowa 50011

Date Transmitted: February 10, 1995

PREPARED FOR THE U.S. DEPARTMENT OF ENERGY
UNDER CONTRACT NO. W-7405-Eng-82.

DISCLAIMER

To my wife, Annika, for her tremendous patience and understanding while I was getting this thing done and my parents for their guidance and support.

TABLE OF CONTENTS

ABSTRACT

With the ever increasing awareness of the toxicity of Pb, significant pressure has been put on the electronics industry to get the Pb out of solder. This work pertains to the development and characterization of an alloy which is Pb-free, yet retains the proven positive qualities of current Sn-Pb solders while enhancing the shortcomings of Sn-Pb solder.

The solder studied is the Sn-4.7Ag-1.7Cu wt% alloy. By utilizing a variety of experimental techniques the alloy was characterized. The alloy has a melting temperature of 217 °C and exhibits eutectic melting behavior. The solder was examined by subjecting to different annealing schedules and examining the microstructural stability. The effect of cooling rate on the microstructure of the solder was also examined.

Overall, this solder alloy shows great promise as a viable alternative to Pb-bearing solders and, as such, an application for a patent has been filed.

1. INTRODUCTION

The most commonly used solders for microelectronic applications today contain an element whose toxicity is widely known and recognized. This element is lead (Pb). The public's awareness of lead's toxicity has recently become more of a factor in restrictive governmental regulation of the element. Tin (Sn) alloyed with Pb produces a eutectic solder alloy which wets and alloys with a host of metals and is by far the most widely used solder alloy. Therefore, governmental regulation of Pb would financially burden the electronics industry.

In addition to the environmental problems of leaded solders there are other problems. Sn-Pb solders are inherently weak and have little resistance to thermal-mechanical fatigue. This is due to Sn-Pb solder's low strength and low eutectic melting temperature, 183 °C. When Sn-Pb solder is used in electronic assemblies which are placed near automobile engines or used in avionics for sensing and control it can undergo temperature cycling between -55 °C and 125 °C (1). Corresponding to 0.5 and 0.9 of the absolute melting temperature of Sn, this is an extreme operating temperature range. Such homologous temperatures are commonly used for hot deformation processing where high diffusivity and plasticity are desired.

It is known that Sn-Ag eutectic solder, the basis for many Pb-free solder candidates, melts at 221 °C and is significantly stronger than Sn-Pb solders. However, these solders are criticized since they do not wet as well and have higher melting temperatures than Sn-Pb eutectic and near eutectic solders. A higher melting temperature is undesirable as far as processing parameters for circuit assembly production is concerned. This study proposes an alloying addition to the Sn-Ag system. This addition should depress the melting temperature, enhance the wetting behavior, have a low cost, be abundant in natural ores and not be a by-product of Pb mining.

2. BACKGROUND

2.1. Brief Introduction to Soldering

Solders have been used for nearly 4000 years. The earliest recorded solder use dates back to the Egypt around 3600 BC (2). Sn-Pb solders have been used for joining since before Roman times. The Sn-Pb eutectic solder (T_m = 183 °C) has withstood the test of time because of its soldering efficiency, relatively low cost, high abundance and good reliability (3). Since humans have had thousands of years experience with solders and soldering one would be led to believe that most of the problems concerning soldering would long be solved. This is a far cry from the truth.

The solution to problems with metallurgically bonding two metals together continue to elude scientists and engineers today. In addition to providing a bonding medium for two metals, soldering provides electrical, thermal and mechanical functions. In the microelectronics industry these functions are vital. Therefore, the integrity of solder joints is essential to the overall performance and reliability of electronic assemblies.

Unfortunately, the number of reported solder failures in industry have risen steadily during the past 30 years. The cause of this continued rise in solder related failures can be due, in part, to the rapid advancement of technology during this same time period, particularly the increase in the use of microelectronics products. Advances in space travel and consumer electronics have increased the number of solder joints which are produced each year. Another factor is the more severe environments in which electronic assemblies are being used, e.g., space, military and automotive. With these applications imposing greater thermal cycling and mechanical stresses, the properties of traditional solders are increasingly inadequate. In addition, it is expected that there will be growing market possibilities in these areas (4).

Within the last decade there has been progress in the areas of materials, processes and equipment used in modern microelectronic soldering. Two key problems remain: the development of a new environmentally safe solder and sharply reducing solder joint failures (5).

2.2. Important Properties of Solders

2.2.1. Wetting and Solderability

Wettability is defined as the tendency for a liquid metal to spread on a solid surface (2). This is a precursor to an important property of any solder: solderability. In the forming of a solder joint it is important that the solder fill in holes and gaps; the solder needs to flow both horizontally and vertically to ensure a solid bond in the joint. Some extrinsic factors which determine how well a solder wets are the time, temperature and flux which are used during the soldering procedure (6).

The contact angle, θ_C, that the molten solder forms at the molten solder-substrate-flux triple point is determined by the balance of the interfacial tensions as given in Equation 2.1.

$$\gamma_{SF}-\gamma_{SL} = \gamma_{LF}\cos\theta_C \qquad (2.1)$$

where γ_{SF} is the substrate-flux interfacial tension, γ_{SL} is the substrate-liquid interfacial tension and γ_{LF} is the liquid-flux interfacial tension (see Figure 2.1*a*). For this model it is assumed that the molten solder and free surface of the substrate are completely covered by a film of liquid flux and no flux is between the liquid solder and substrate (7, 8) .

When comparing the performance of different solders or fluxes the contact angle provides the best indicator for the performance of the material in question (2). Some wettability parameters for two solders, Sn-37Pb and Sn-3.5Ag (both eutectic compositions in

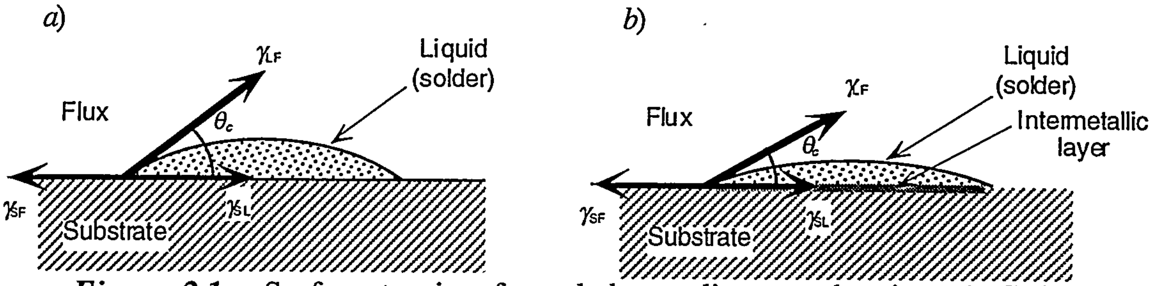

***Figure* 2.1** Surface tension force balance diagram showing *a*) Cu/solder interface with no intermetallic layer and *b*) Cu/solder interface with an intermetallic layer.

wt%) at 260 °C are given in Table 2.1. A lower contact angle indicates better wetting behavior. The higher contact angle of the Sn-3.5Ag solder has been attributed to the absence of Pb. It is believed that Pb lowers the liquid solder-substrate interfacial tension, γ_{SL}, thus decreasing θ_c.

Table 2.1 Contact angle of two solders on a copper substrate (2).

Solder	Contact Angle, θ_c
Sn-37Pb	17 ± 4
Sn-3.5Ag	36 ± 3

Wetting is promoted by small values of γ_{SL} and γ_{LF} in combination with a relatively large value of γ_{SF}. Another important thermodynamic relation is the Gibbs Relation which states that any spontaneous change in the interface which separates two given phases lowers the interfacial tension ($\Delta\gamma \leq 0$) (9). The change which occurs in the soldering process, which is typically a liquid Sn-based alloy in contact with a Cu substrate, is the spontaneous formation of intermetallic compounds, i.e., Cu_3Sn and Cu_6Sn_5. As a result of the formation of these compounds the surface tension between the liquid solder and the newly formed intermetallic compound, γ_{SL}, is lowered thus decreasing the contact angle, θ_c, compared to the liquid solder on a pure Cu substrate (see Figure 2.1*b*).

Wetting is also a strong function of the flux that is used for the soldering application. Fluxing the surface of the substrate, usually Cu, removes the oxide layer and allows the liquid solder to come into contact with the bare metal. Commonly used fluxes are rosin mildly activated (RMA), "no clean", and water soluble fluxes (6, 10-13) Flux selection depends on solder/substrate combination, soldering temperature and atmosphere.

2.2.2. Melting Temperature

For microelectronics applications a solder's melting (or liquidus) temperature affects soldering process parameters and the service environment where the solder joint will be used. It is common to have the soldering process temperature (wave solder bath, surface mount technology, (SMT) reflow oven, etc.) set to 50 °C above the melting or liquidus temperature of the solder (14). Since the most common solders used are based on the Sn-Pb eutectic composition which has a melting temperature of 183 °C, the process operating temperature is generally around 230 °C. This superheat insures that wetting and spreading be sufficiently fast in order to achieve a successful solder joint on the first pass. The spreading of the solder is defined as the ability of the solder to fill the solder joint. In general, some superheating is needed to enhance the kinetics of the wetting and joint filling processes. Microelectronic assembly manufacturers are apprehensive of any solder which has a melting temperature higher than 183 °C since this would mean adjusting current processing parameters. If the processing temperature is higher than about 230 °C for a reflow process then questions such as the integrity of the circuit board and components must be examined as well as the adjustment limits of the processing ovens.

Higher melting temperature solders have found use, however, in severe service environments such as automotive or avionic applications. The operating temperatures of these environments can be as high as 150 °C (15). Since this temperature is 0.9 of the absolute melting temperature of Sn-Pb eutectic and near eutectic solders these solders are not suitable because of their low strength and resistance to fatigue at these temperatures.

2.2.3. Intermetallic Morphology

Intermetallics which form in the bulk of Sn-Ag based Pb-free solders generally are either rounded or needle-like in morphology. The intermetallic morphology can be important when considering the performance of a solder. If the intermetallics' morphology is needle-like the stress concentrations at the tips of the needles will be prone to induce cracks during thermal-mechanical fatigue which will ultimately lead to mechanical and electrical failure of the joint. If the intermetallics are rounded and evenly dispersed throughout the matrix, they could actually enhance the overall strength and fatigue resistance of the solder.

2.2.4. Mechanical Properties

The main purpose of a solder is to provide an electrical bond between circuit board contact and microchip lead. A solder must also provide a mechanical bond. If the mechanical bond becomes ruptured the electrical contact is also interrupted. The strength of a solder is important to the solder's overall performance.

2.2.5. Cost

The microelectronics industry cannot escape financial considerations. When considering a substitute of a new Pb-free solder alloy for a particular application the cost is a very important factor to consider. However, solder alloy cost becomes less significant in the rapidly growing SMT assembly industry which uses solder paste, a blend of solder alloy powder with a fluid flux solution. For example, raw materials cost for typical Sn-37Pb solder is $2/lb. while pastes with this alloy range in price from $63-$108/lb. Sn-5Ag alloy cost is about $5-$6/lb while Sn-Ag solder pastes typically sell for $72-$138/lb (16). A new Pb-free solder should be on par with these costs if it is to be worthy of serious consideration.

2.3. Toxicity of Leaded Solders

The most widely used solders contain Pb. Pb is a known toxin and can be considered a serious public health threat. Recent studies have linked Pb blood (PbB) levels in children to learning and behavioral disorders. Since the banning of Pb in gasoline, average PbB levels have decreased 87% (17). This is encouraging since it supports the claim that regulatory action can indeed generate a substantial improvement in environmental quality. Other legislation in congress has threatened to ban or heavily tax the use of Pb in all industries (18). Such a tax would heavily burden US solder and electronics manufacturers until equivalent laws are enacted in other industrialized countries or a viable Pb-free solder substitute is developed.

Pb waste in the electronic industry is formed in two ways: during the assembly of circuit boards (industries) and in the disposal of these assemblies (consumers). In the first case waste is mainly found in the solder dross, which can contain 96-98% metals (19). Since dross can create Pb containing dust, its handling is controlled by the US Occupational Safety and Health Administration (OSHA) and is strictly regulated (2).

To date, no scientific data have demonstrated that consumer disposal of Pb-bearing solders in electronic assemblies are a toxic hazard to the environment. But the environmental protection agency (EPA) has estimated that the amount of Pb entering public landfills from discarded television sets, computers etc. exceeded 50,000 tons in 1990 (20). The Pb in these products originates in the solder used in circuit boards and in the leaded glass cathode ray display screens. There have been several proposals to ban the use of all Pb bearing materials in manufacturing. The original Toxic Lead Reduction Act of 1990 would have banned the use of all Pb-bearing solders (21). After intense lobbying against the bill by electronics manufacturers the bill was rewritten to exclude electronic solders (3).

Environmental restrictions have also been proposed in reaction to voluminous studies within the last 20 years which have associated PbB levels to behavioral disorders and lowering of intelligence in children (22-34). In the early 1970's the highest acceptable PbB levels in children was considered 60 µg/dL but today PbB levels as low as 10 µg/dL are associated with adverse effects on children such as decreased intelligence and impaired neurobehavioral development. Other effects which are believed to begin at these low blood levels are decreased stature or growth and decreased hearing keenness (34) . It is now known that large numbers of children may be afflicted with various adverse health problems at PbB levels that were once considered safe. Costwise, by avoiding PbB levels above 24 µg/dL a total of $4600 can be saved per child (33) in public health and special health care services.

An example of proposed economic actions against all Pb bearing products is the Lead-Based Paint Hazard Abatement Act (35). This act would impose a $0.75 per pound ($1.65/kg) tax on primary refined Pb and $0.37 per pound ($0.82/kg) tax on secondary refined Pb, irrespective of its final use. The EPA has also released documents pertaining to the toxicity of Pb. With increased concern over the environmental impact of Pb it is clear that a new Pb-free solder must be scrutinized for its environmental fingerprint (2).

2.4. Mechanical Insufficiencies of Pb-bearing Solders

The Sn-Pb eutectic microstructure consists of β–Sn and Pb, both of which have low strength. The prime cause of solder joint failure in electronics applications is low-cycle fatigue (36). The large stresses which cause fatigue failures result from the difference of the thermal expansion coefficients of the board and components and thermal gradients across the solder joint (15). When a low strength solder such as Sn-37Pb is used in applications with enhanced cyclic stresses induced by thermal expansion mismatch and wide variations in operating temperature, failures can result.

Stresses in solder joints in electronic assemblies are more important today than ever before. With the advent of surface mount technology (SMT), solders are being subjected to higher stresses. In the past, electronic assemblies employed components which contained wire leads that were through-hole soldered to the printed wiring board (PWB) (see Figure 2.2*a*). The wire was designed to accept the burden of stresses resulting from the difference in the coefficient of thermal expansion (CTE) between chip carrier and circuit board (1). The solder's stress was minimized with this approach. A typical ceramic chip carrier has a CTE of 6 (10^{-6})/°C and an epoxy impregnated fiberglass circuit board's CTE is 15 (10^{-6})/°C (37). In SMT however, particularly in the leadless chip carrier design, the solder takes up much more of the strain due to the CTE mismatch between chip and board (1) (see Figure 2.2*b*).

The low strength and resistance to thermal-mechanical fatigue of Sn-Pb solders has been widely studied. The as-cast Pb-Sn eutectic microstructure is composed of Pb rich dendrites surrounded by eutectic colonies (lamellar and globular) of Pb-rich and Sn-rich phases (12, 36, 37). Upon solidification these colonies and dendrites grow into the molten solder. Near the middle of the joint the colonies intersect and are the last regions to solidify. The intersections of different growing colonies results in heterogeneous regions which are coarse compared to the structure inside the colonies (1). Upon thermal cycling coarsening

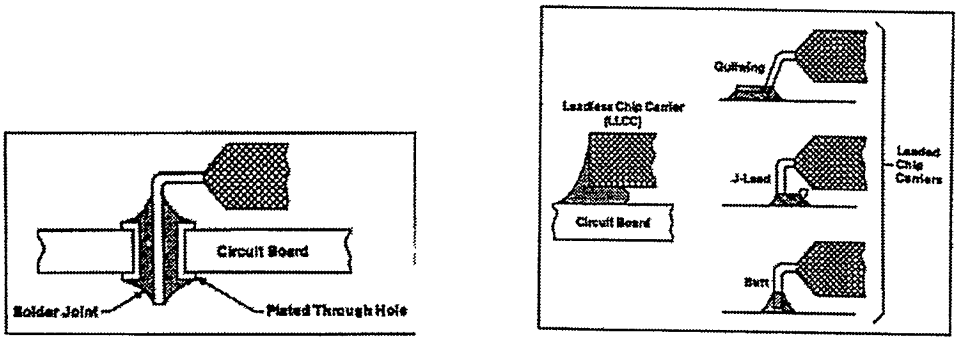

a) *b)*

Figure **2.2** Schematic of leaded and leadless chip carriers used in surface mount technology (15) *a)* through hole joint and *b)* SMT joint.

continues in these regions. Crack initiation during thermal-mechanical fatigue has been found to begin in coarsened regions of the solder's microstructure. The areas which are coarsened in the Pb-Sn eutectic are weaker than areas which have not coarsened (38).

Hence, the inherent low strength and resistance to thermal-mechanical fatigue of Sn-Pb solders can indeed be improved upon. If an improved Pb-free solder were developed which had higher strength, resisted coarsening and had good solderability this would prove valuable to the microelectronics industry.

2.5. Shortcomings of Current Pb-free Solders

Most assembly production parameters are currently set for a solder which melts at 183 °C. As stated earlier, typical operating temperatures generally are about 50 °C above the solder's liquidus temperature or about 230 °C (14). If a new solder with a significantly higher melting temperature is used, this will necessitate re-evaluation of the complete soldering process including cleaning, flux, components, substrates and manufacturing methodology (39). If a solder with a slightly higher melting temperature were used the assembly process could be altered within acceptable limits to accommodate a higher melting solder.

The wetting behavior of current Sn-Ag based Pb-free solders are inferior to currently used Sn-Pb based solders. However, the solderability may be enhanced by adjusting the flux chemistry used with the solder or with ternary alloying additions to the Sn-Ag base alloy. A ternary alloying addition can also reduce the melting point of the Sn-Ag alloy.

2.6. Advantages of Current Pb-free Solders

The higher melting temperature (with respect to Sn-37Pb) of Sn-Ag solders permits the solder to be used in more severe environments, e.g., avionics and automotive, where current Sn-Pb solders have proven unreliable. More importantly, the greater strength of Sn-Ag solders compared to Sn-Pb solders, irrelevant of temperature, is advantageous. The intermetallic secondary phases in Sn-Ag solders help strengthen the solder and improve resistance to thermal-mechanical fatigue. At room temperature, the tensile strength of Sn-40Pb is 40 MPa (40) while the tensile strength of Sn-3.5Ag is 60 MPa (41).

2.7. How to Improve on Sn-Ag Solder

There are two major shortcomings of current Sn-Ag based Pb-free solders: they have a higher melting temperature and do not wet Cu as well as Sn-Pb based solders. However, Sn-Ag based solders have much higher strengths when compared to Sn-Pb based solders. To overcome the aforementioned shortcomings of the Sn-Ag solder, it could be alloyed with a ternary alloying addition. This approach would be most advantageous if a ternary eutectic alloy was discovered. A suitable ternary eutectic Sn-Ag based alloy should have a lower melting temperature than the Sn-3.5Ag binary eutectic and should have a more refined microstructure, avoiding the formation of Sn dendrites (42).

When considering alloying additions, the following criteria were selected: *i*) reduced toxicity compared to Sn-Pb solders (including not being a part of the Pb mining cycle), *ii*) availability (world capacity), *iii*) low cost, *iv*) enhances solderability of Sn-Ag, and *v*) moderately low ternary melting temperature (from the published ternary phase diagrams). Several possible alloying additions that are known to depress the melting point and to form a eutectic with pure Sn are Bi, Cu, Ga, In, Sb and Zn. The electronics solder market consumes an estimated 60,000 tonnes of Sn-Pb solder per year (14). Even a 1 wt% usage of one of these elements would generate a demand for 600 tonnes per year. Hence, world capacity is definitely an important consideration. Of the aforementioned elements, Cu and Zn meet the above criteria and are the most abundant (see Table 2.2). However, there are two reasons why Zn has been avoided as a solder alloying addition: *i*) even in small concentrations Zn in the liquid state is known to react readily with air and *ii*) Zn is susceptible to corrosion (43). This leaves Cu as the optimum alloying addition to be investigated in this study. Since Cu also depresses the melting point of pure Ag and forms a simple eutectic without compounds, it was conceivable that a Sn-Ag-Cu ternary eutectic may also exist.

Table 2.2 Availability of potential alloying elements (14).

Element	Annual World Production (tonnes)	Annual World Capacity (tonnes)
Ag	13,500	15,000
Bi	4000	8000
Cu	$8\text{x}10^6$	$10.2\text{x}10^6$
Ga	30	80
In	80-100	200
Sb	78,196	122,300
Sn	200,000	281,000
Zn	$6.9\text{x}10^6$	$7.6\text{x}10^6$

3. APPROACH

3.1. Characterization of the Sn-Ag-Cu Eutectic Alloy

A main objective of this work was to determine whether or not a ternary eutectic reaction had been overlooked in the Sn-Ag-Cu system and, if identified, to investigate the ternary eutectic alloy's behavior in some simulated solder processing applications. Once the ternary eutectic composition and temperature of the system were determined, additional practical aspects of the solder were investigated.

Initially, the effect on the solders microstructure of the temperature and time at temperature when casting the solder was examined. This is important since the solder is composed of elements which vary greatly in melting temperature, from 231 °C (Sn) to 1085 °C (Cu). For industrial practice a minimum time and temperature for casting the alloys must be determined to minimize manufacturing cost and to allow for complete alloy homogenization. Another important parameter in electronic assembly manufacturing is the cooling rate the solder joint is subjected to when the joint is made. The cooling rate will determine how refined the solder's microstructure is and, ultimately, how the solder will perform in demanding applications. Also, in the design of valid mechanical properties tests, knowledge of the solder's initial microstructure is essential. Therefore, the correlation of cooling rate to the solder's microstructure was investigated. To understand how stable the ternary eutectic alloy's microstructure is in a high temperature application, the hardness and stability of the solder's microstructure were studied as a function of different annealing temperatures and times.

3.1.1. Phase Diagram Determination

After examination of the published Sn-Ag-Cu phase diagram (44), alloy samples of various compositions in the Sn-rich region of the Sn-Ag-Cu system were chill cast (see

Figure 3.1). A sample of Sn-3.6Ag-1.5Cu wt% (corresponding to the previously published four-phase equilibrium composition) was also cast. The eutectic microstructure regions present in this sample were analyzed for compositional information to estimate the true four-phase equilibrium composition. The new four-phase equilibrium eutectic composition was then verified with microscopy, x-ray diffraction and DTA.

Further phase diagram determination included experimental examination of the melting behavior of ternary eutectic and near eutectic alloys in the Sn-rich region of the phase diagram. Emulsified samples of varying compositions were analyzed using DTA. By measuring solidus and liquidus temperatures of two isopleths, the eutectic composition was confirmed through extrapolation of the liquidus curves. X-ray diffraction was also used to verify the presence of the three phases which compose the ternary eutectic.

DTA is a widely used and proven method of phase diagram determination (45-54). By examining the endothermic peaks of the DTA heating curves both solidus and liquidus temperatures were determined. An alloy of eutectic composition will have a single melting event resulting in a single, continuous peak on the DTA heating curve. An alloy of off-eutectic composition will have both a solidus and liquidus transition resulting in two peaks in the DTA heating curve or, if the two peaks overlap, one discontinuous DTA curve.

3.1.2. Casting Conditions

A problem concerning the casting of the Sn-Ag-Cu solder alloys was to determine the casting temperature and time at temperature which would be adequate to provide complete dissolution of the elements. To determine casting conditions which would provide complete alloy homogenization, several samples of Sn-4.7Ag-1.7Cu wt% composition were chill cast at different temperatures for different times. By analyzing the microstructure of these alloys for undissolved portions of the original elements it was determined which casting parameters were acceptable. This has important ramifications for industry practices by determining a sufficient, yet minimal, time and temperature for casting.

3.1.3. Cooling Rate Study

In the manufacturing of solder joints for circuit board assemblies there are many different soldering processes, e.g., wave, through-hole, and SMT. In each of these different methods, the solder is subjected to different cooling rates. The effect of cooling rate on the microstructure was studied, since ultimately the solder's microstructure has a strong influence on its mechanical properties. The cooling rate study was carried out by melting small beads of solder on a Cu plate and then cooling the solder in different environments.

Each solder sample was then examined using a scanning electron microscope to determine the spacing of the eutectic matrix and the amount and location of intermetallic formation outside of the eutectic matrix. The micro-hardness of each solder sample after being cooled at different rates was also measured. By correlating these measured hardnesses to the hardness of solder subjected to different soldering processes (e.g., through hole joints and wave soldering) the cooling rate for each soldering process may be estimated.

3.1.4. Microstructural Stability

Hand solder joints were made on a test circuit board. Individual through-hole solder joints were then annealed for various times and temperatures. By examining the microstructures of the annealed solder joints, information concerning the growth rate of dispersed intermetallic phases in the solder bulk could be obtained. This would indicate how the solder would perform in applications where the operating temperature would be elevated. The morphology (i.e., spheroidal vs. faceted) and size of the coarsened dispersed secondary phases provided an indication of the resistance to crack initiation during thermal mechanical fatigue.

The annealed solder joints were also micro-hardness tested. The retained strength of the annealed solder could be estimated by inspecting the retained hardness after annealing.

3.2. Experimental Procedures

Characterization of the Sn-4.7Ag-1.7Cu wt% solder alloy was carried out by utilizing such diverse methods as metallography, wavelength dispersive spectrometry (WDS), x-ray diffraction, scanning electron microscopy (SEM) and differential thermal analysis (DTA). An emulsification process was also employed to produce fine powders for DTA. This section describes these procedures as performed in this work.

3.2.1. Chill Casting Procedure

As an initial step, 25 g samples of varying Sn-Ag-Cu composition were cast. First, each of the individual elements were etched: Cu with 35 vol% nitric acid in water; Sn with 30 vol% HCl in water; Ag with a 5:3 (by volume) mixture of ammonium hydroxide:hydrogen peroxide. After etching, each element was rinsed in water and acetone and ultrasonically cleaned in methanol for 5 minutes and air dried. Finally, each element was weighed on an electronic microbalance to within ± 0.50 mg of the target weight.

A 6 mm inner diameter by 45 cm long Pyrex tube was fused to a 6 mm diameter by 30 cm long Pyrex rod which provided a convenient way to handle the tube. The tube was rinsed with acetone and methanol and allowed to air dry. When the proper ratio of elements was obtained, the elements were placed in the Pyrex tube. Next, the tube was secured to a vacuum pump and evacuated to ≈ 50 millitorr and outgassed by heating it over an open oxy-methane flame. The tube was backfilled with He and pumped down for 3 cycles waiting approximately 10 minutes between each cycle and, finally, backfilled to 0.5 atm pressure with He and sealed with an oxy-methane flame (see Figure 3.2). Each sample was then typically heated to 650 °C for 45 minutes while being severely agitated every 10 minutes by

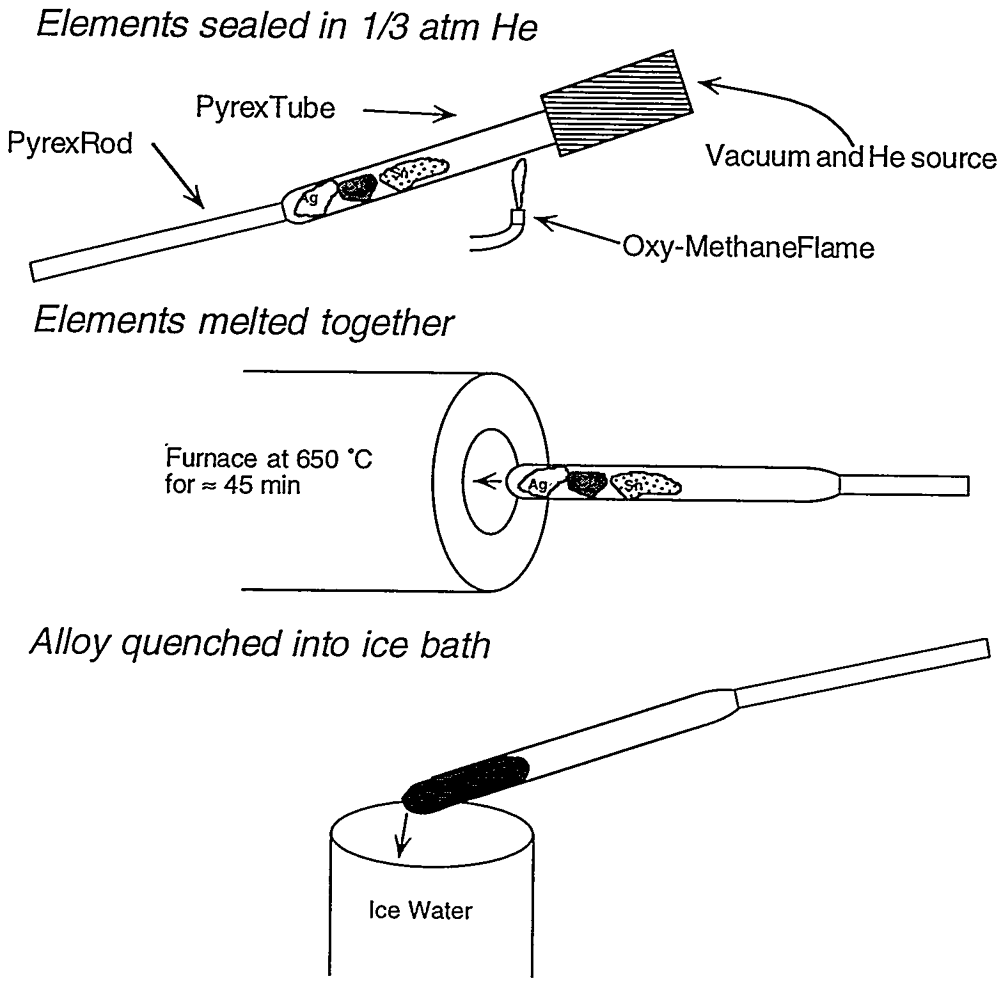

***Figure* 3.2** Schematic diagram of chill casting procedure.

rocking the tube end over end. It was then cooled rapidly by dipping the Pyrex in an ice-water bath (Figure 3.2) until the Pyrex had adjusted to the temperature change at which time the Pyrex tube was completely immersed. After the surface appearance of the alloy sample indicated that solidification was complete, the tube was cracked open. The ingot sample was then labeled and stored.

3.2.2. Optical and Scanning Electron Microscopy

Selected 25 g cast alloys were analyzed with optical microscopy. Samples were sectioned with a diamond saw, mounted in epoxy-resin, ground on 320 and 600 grit SiC paper, polished on a 0.1 diamond slurry and, finally, polished on a 0.05 μm alumina slurry. Samples were examined with an optical microscope in both the etched and unetched condition. The eutectic microstructure and intermetallic phases became more visible after etching in a solution of 2 vol% hydrochloric acid in methanol. Optical microscopy was used to obtain low magnification (50-1000x) micrographs. Optical micrographs were taken using Polaroid 667 film.

Scanning electron microscopy (SEM) was performed on bulk samples. The SEM was set at an accelerating voltage of 15 kV, objective aperture was set to 2. SEM micrographs were taken with Polaroid 55 film.

In addition to the standard polishing procedure, the SEM samples required an additional step. In order to hinder charging of the epoxy mount, the surface of the sample which contained epoxy was made conductive by one of two methods: concealing the epoxy surface with copper adhesive tape or carbon sputtering the entire sample surface. The copper tape method invariably left exposed epoxy areas near the mounted sample. The carbon sputtering method worked much better than the other method because no epoxy areas were left exposed (see Figure 3.3).

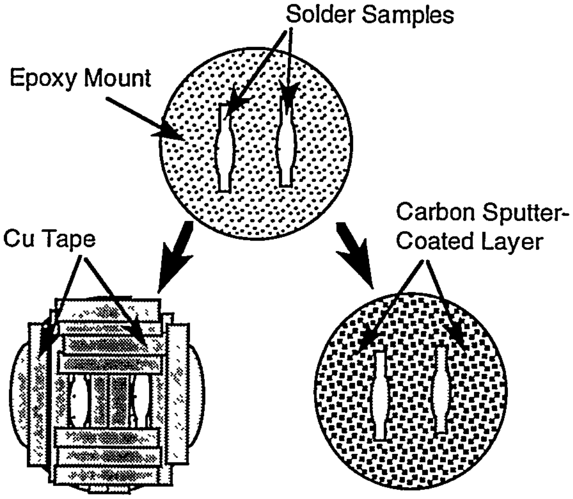

Figure 3.3 Schematic diagram showing the initial mount with solder samples (top) and the resulting mounts after covering epoxy with Cu adhesive (left) and carbon sputtering (right).

3.2.3. Wavelength Dispersive Spectrometry (WDS)

Wavelength dispersive spectrometry (WDS), or microprobe analysis, provided quantitative composition information on the eutectic microstructure present in an off-eutectic sample. Eight WDS runs were performed on an unetched, polished section of the 25 g cast Sn-3.6Ag-1.5Cu wt% sample, the composition of the previously reported $L + \eta \Rightarrow \theta + \beta$-Sn reaction. The sample was mounted using the same procedure as the optical microscopy samples, see section 3.2.2. The eutectic solidification microstructure regions in the sample were large enough (>30 μm) for WDS measurements to be made. Eight runs were performed on eight different eutectic regions. The WDS data were recorded from area scans using between 32 and 100 data points per run.

The Sn, Ag and Cu used for calibrating the WDS apparatus were from the same stock of the elements used in the sample and were in a different mount than the sample. The WDS analysis was performed with a 30 mA filament current and a 20 kV accelerating voltage. The apparatus was equipped with three scanning spectrometers; one was used for the detection of

Cu, one for Sn and Ag and one was idle. The x-ray energies emitted from Sn and Ag are close enough so that only one detector was used for both elements. The raw data collected were corrected with the ZAF (atomic number, absorption and fluorescence) method.

3.2.4. Emulsification

Emulsions of metal droplets suspended in an oil-surfactant mixture were created from 1 g samples of each chill cast ingot. Emulsified samples on the order of 5-20 mg were used for DTA. To better ensure homogeneity in the DTA samples, 1 g pieces were cut from the chill cast ingots and emulsified into fine droplets. These fine droplets were subjected to DTA in 5-20 mg portions. Since each emulsified droplet came from a relatively large 1 g portion of the cast ingot, each droplet has a high probability of having the same composition as the cast sample. In contrast, if a solid 5-20 mg DTA sample was cut directly from the ingot, the composition of the sample would not be exactly known due to the possibility of segregation and inhomogeneity in the cast ingot.

The emulsification apparatus (55) consisted of a variac, variable speed Dremel tool with attached mixing blade, a threaded Pyrex tube, a source of Ar gas, a band heater, a mullite tube, glass fiber, a Chromel-Alumel thermocouple and a temperature controller, Figure 3.4. The construction and operation of the emulsification apparatus is outlined below.

The blades and shaft were constructed out of stock 3/16" (0.476 cm) diameter 304 stainless steel rod. After cutting the rod to a 15 cm length, two slits were made in one end with a Dremel tool using a cutoff blade. The four prongs which remained were bent back to form the blades, Figure 3.4. The lower blades were tilted at an angle about 45° to the horizontal to provide upward circulation and the top set of blades were sharpened to shear the liquid metal in the carrier fluid. The blades were shortened with the Dremel tool so they would fit inside the Pyrex tube. Before cutting the blade shaft to the final length, the Pyrex tube and aluminum coupler were made so the necessary length of the shaft could be determined. After the shaft length was determined, the shaft was cut to the correct length. Finally, the top of the blade shaft was machined in diameter so that it would make an interference fit with the chuck of the Dremel tool. Before inserting the shaft into the Dremel tool, Duco cement was applied to the end of the shaft to ensure a lasting fit.

The blade shaft was balanced so that high speeds of 30,000 rpm could be obtained without deforming the shaft. Balancing was done by turning on the Dremel and lightly touching the spinning shaft with a pencil. Only one side of the shaft comes into contact with the pencil if it is out of balance. After the Dremel was turned off, the shaft was carefully bent away from the side with the pencil mark. This was done repeatedly until the Dremel could be turned up to full speed with the shaft remaining balanced. The shaft would become slightly out of balance in a certain resonant speed range but become balanced again at higher speeds. The resonant speed range was heard as a groaning sound of the Dremel tool. If the shaft speed was rapidly increased through the resonance speed range, the shaft would quickly become balanced again. In contrast, if the speed was only slowly increased through this range the shaft would become more unbalanced and be unusable.

A variable amperage power supply supplied the Dremel tool with current. This allowed control of the Dremel tool at low speeds which was otherwise impossible with the built in speed control. The power supply also delivered more current to the motor than the built-in speed control alone, thereby providing a higher maximum speed.

Each threaded Pyrex tube was reshaped to enhance the efficiency of the emulsifier apparatus. The stock Pyrex tube was initially 125 mm long by 12 mm diameter and was shortened to 10 cm. The bottom of the 10 cm long Pyrex tube was formed into a four-leaf clover shaped cross-section. This was performed by heating the bottom of the Pyrex tube in an oxy-methane flame and making four indents on the side at the bottom with a small spatula. The four-leaf clover cross-section prevented the heavy liquid metal droplets from simply circulating against the wall of the Pyrex tube (see Figure 3.5).

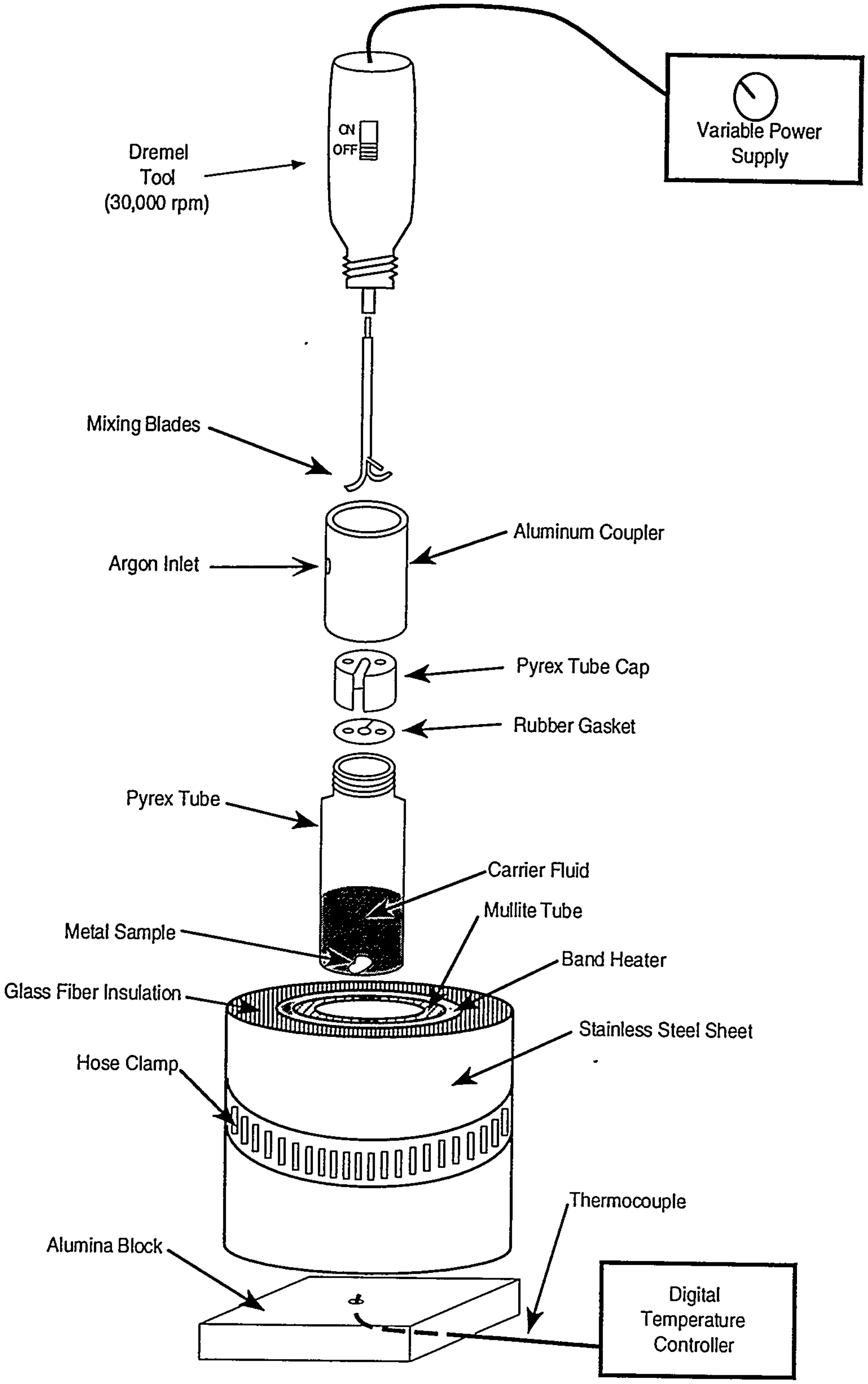

Figure 3.4 Schematic diagram of emulsifier apparatus (exploded view).

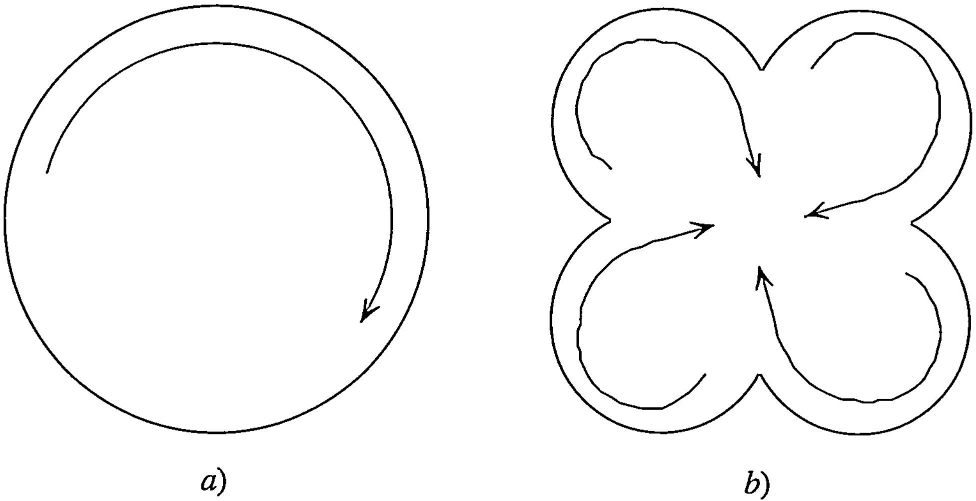

a) *b*)

***Figure* 3.5** Schematic of emulsion mixing action in bottom of Pyrex tube: *a*) clover leaf cross section vs. *b*) circular cross section.

The heating element of the emulsifier apparatus consisted of a 550 W band heater surrounded by a mullite tube, glass fiber filling and a stainless steel sheet, thus composing a "furnace" which could be moved as one unit (see Figure 3.4). The furnace rested on an alumina block. The thermocouple protruded up from the center of the alumina block 1 inch into the furnace.

The aluminum coupler connected the Pyrex tube to the Dremel tool and contained an inlet for the Ar purge gas. The top of the coupler was machined to match the threads of the Dremel tool. The screw on cap of the Pyrex tube was fit inside the bottom of the coupler and held in the coupler by three thumb screws. A slot was drilled into the screw cap which allowed the cap to be placed in the aluminum coupler after the blade shaft was attached to the Dremel. A slit was cut into the rubber gasket, as well. Two holes were drilled into both the cap and rubber gasket as shown in Figure 3.4. The holes allowed the Ar gas to flow into the Pyrex tube and provide a cover atmosphere for the liquid metal and carrier fluid. The 99.99% pure Ar gas was directed into the coupler via a tube with a needle on the end.

The carrier fluid-surfactant mixture (100:1 by weight of tricresyl phosphate [$(CH_3C_6H_4O)_3P(O)$]:phosphotungstic acid [$H_3PO_4 \cdot 12WO_3\ XH_2O$]) and the 1 g bulk chill cast sample were placed in the Pyrex tube (55). The Pyrex tube was attached to the coupler and the Ar gas was turned on. The Ar purge gas prevented the metal from oxidizing as the system was heated. The Pyrex tube was lowered so it was fully inside the band heater. The temperature controller was set for 300 °C. When the metal piece had melted the Dremel tool was set at high for 10-20 seconds. The Dremel tool spun the mixing blades at about 30,000 rpm. It was then turned off and the Pyrex tube was raised out of the band heater.

The emulsified droplets were allowed to solidify and transferred to a test tube with a pipette. The surface of the droplets reacted with the surfactant so that droplet coalescence during settling of the emulsion was prevented. The metal droplets were then rinsed in acetone and ultrasonically cleaned in methanol to remove the emulsification oil. The droplets were then filtered with 11 μm filter paper and allowed to air dry yielding a fine powder. The powders were used as DTA samples to determine the liquidus and solidus temperatures of the different alloys.

3.2.5. Differential Thermal Analysis (DTA)

Differential thermal analysis (DTA) provided accurate determination of liquidus and solidus temperatures of the 5-20 mg powder samples. The apparatus used was a computer controlled Perkin-Elmer DTA-7. Each powder sample was weighed and put in a small alumina cup and covered with alumina powder. The reference sample was alumina powder in an alumina cup. Each sample was taken from 200 °C to 240 °C at a very slow heating rate of 0.1 °C/min, for good sensitivity. During heating the sample chamber was purged with 99.99 % pure Ar gas flowing at 50 cc/min.

3.2.6. X-ray Diffraction

X-ray diffraction was performed on a chill-cast and sample of Sn-4.7Ag-1.7Cu wt% using a Scintag diffractometer and Cu K_α radiation. The scans were performed from 2Θ = 20-80° at 1 °/min with a step size of 0.03°. The powders were mounted on a glass slide using silicone vacuum grease. The glass slide was then affixed to the sample holder with an amorphous solid (Apezion Q). The bulk sample was simply affixed directly to the sample holder using an amorphous solid. The sample was then leveled with the surface of the sample holder to provide proper alignment in the diffractometer. The x-ray analysis determined the structural identity of the phases that WDS and optical microscopy indicated were present in the Sn-4.7Ag-1.7Cu wt% alloy.

4. RESULTS

4.1. Phase Diagram Determination

Published Sn-Ag-Cu phase diagram data (44) indicated that a ternary reaction occurs in the Sn-rich region of the Sn-Ag-Cu system (Sn-3.6Ag-1.5Cu wt%) at 225 °C as a class II four-phase equilibrium reaction ($L + \eta \Rightarrow \theta + \beta$-Sn, $\eta = Cu_6Sn_5$, $\theta = Ag_3Sn$) (56). In the earlier study only one alloy sample was investigated in the Sn-rich region of the Sn-Ag-Cu system: Sn-5Ag-5Cu (wt%). In contrast to the earlier study, this work included a large set of Sn-rich ternary alloys, 11, and the characterization results were improved by utilizing modern microstructural, chemical and thermal analysis methods.

The lowest melting point of the system, i.e., a ternary eutectic composition was sought out. If, in fact, a ternary eutectic exists in the Sn rich region, one would expect the reaction to be $L \Rightarrow \eta + \theta + \beta$-Sn. As a starting point, a sample of Sn-3.6Ag-1.5Cu wt%, corresponding to the previously published phase diagram class II ternary composition, was chill cast. The sample was then mounted, polished and lightly etched. The sample was then examined using an optical microscope. This revealed an apparent eutectic phase penetrated by β-Sn dendrites (see Figure 4.1*a*, *b*). Because the areas with eutectic microstructure were on the order of 30 μm in diameter, see Figure 4.1*b*, these areas were analyzed using WDS to estimate the ternary eutectic composition.

The WDS compositional results are summarized in Figure 4.2. The average composition for each element was calculated for each run. The average of each run was averaged together yielding a grand average composition of Sn-4.7Ag-1.7Cu wt%, shown by the lines on the *y* axes. Adding the elemental weight percents for a given run yielded a number which was less than 100%. To normalize the sum of the weight percents to 100, each element's measured weight percent was divided by the sum of the measured weight percents. Figure 4.2 is a plot of normalized elemental compositions.

An alloy of Sn-4.7Ag-1.7Cu wt% was chill cast and examined to determine if this could be the ternary eutectic composition. Optical microscopy performed on this sample revealed a microstructure composed almost entirely of eutectic, see Figures 4.3*a*, *b*. Eutectic colonies composed of what appeared to be a lamellar microstructure are visible in Figure 4.3*b*.

X-ray analysis performed on a solid Sn-4.7Ag-1.7Cu wt% chill cast sample indicated that three phases were indeed present, Figure 4.4. The Bragg reflections present were indexed as belonging to β-Sn (bct), Ag_3Sn (orthorhombic) or Cu_6Sn_5 (hexagonal). These phases were expected to be present in the ternary eutectic microstructure according to the reaction $L \Rightarrow \eta + \theta + \beta$-Sn. The x-ray diffraction results support the WDS and microscopy observations.

The compositions of the remaining cast samples were selected by drawing two isopleths extending from the Sn-x (x = Ag, Cu) binary eutectics through Sn-4.7Ag-1.7Cu wt% on a liquidus projection of the Sn-Ag-Cu phase diagram (see Figure 4.5 and Table 4.1). Evenly spaced points were then picked along these lines corresponding to the composition of samples which were cast, emulsified and analyzed using DTA. DTA provided solidus and liquidus temperatures of the two isopleths.

DTA was performed on emulsified samples to determine the onset of melting and the liquidus temperatures, if present, and the results are given in Table 4.2. The samples were labeled as PDM*x* for phase diagram mapping. From these results, isopleths were plotted as shown in Figure 4.6. These isopleths correspond with the lines drawn on the liquidus projection of Figure 4.2. The actual DTA thermograms obtained for the DTA runs are shown in the Appendix in Figures A1-A11.

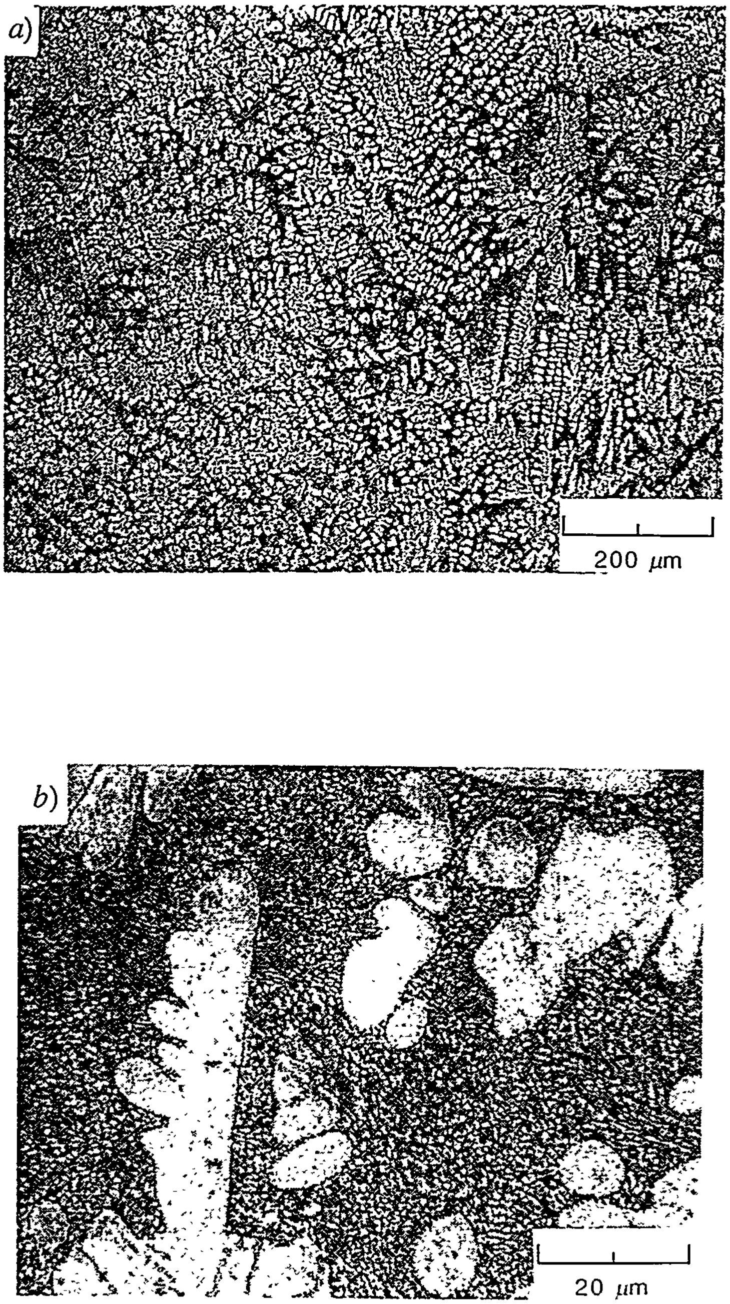

Figure 4.1 Optical micrographs of Sn-3.6Ag-1.5Cu wt% chill cast sample etched with 2 vol % HCl in methanol. *a*) dark contrast eutectic matrix penetrated by β-Sn dendrites, *b*) high magnification of *a*).

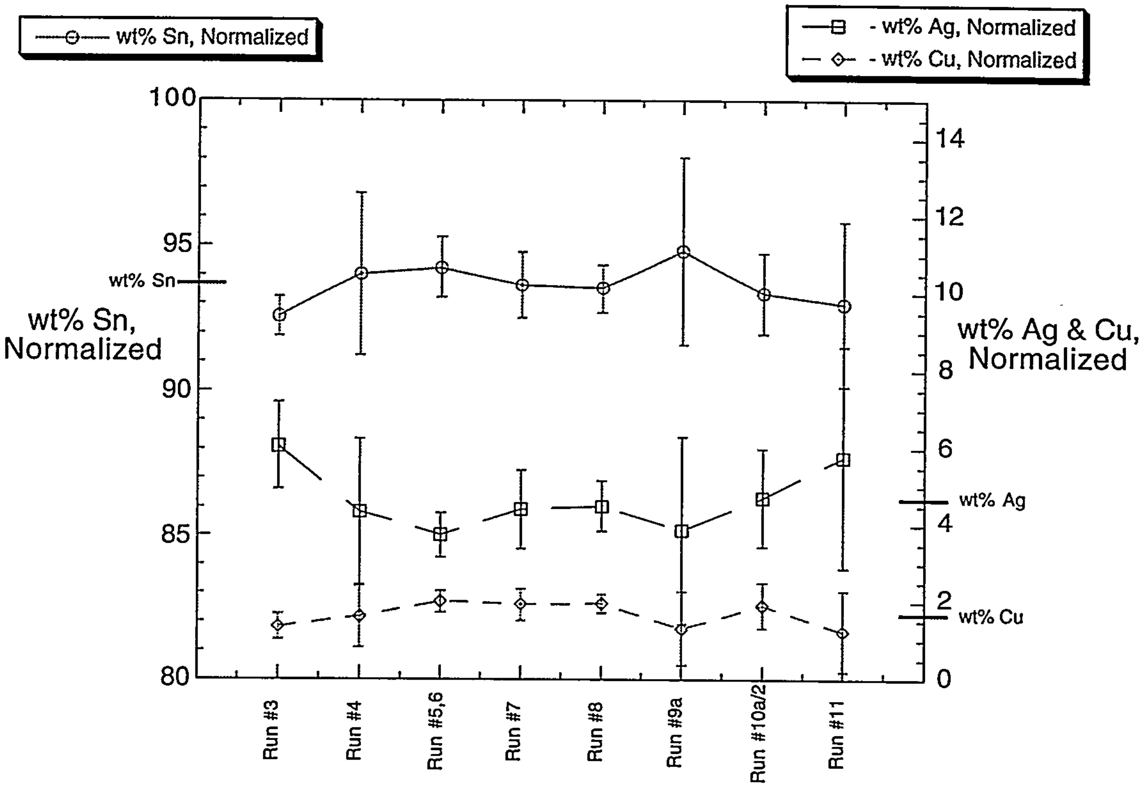

Figure 4.2 Summary of results of WDS run measurements.

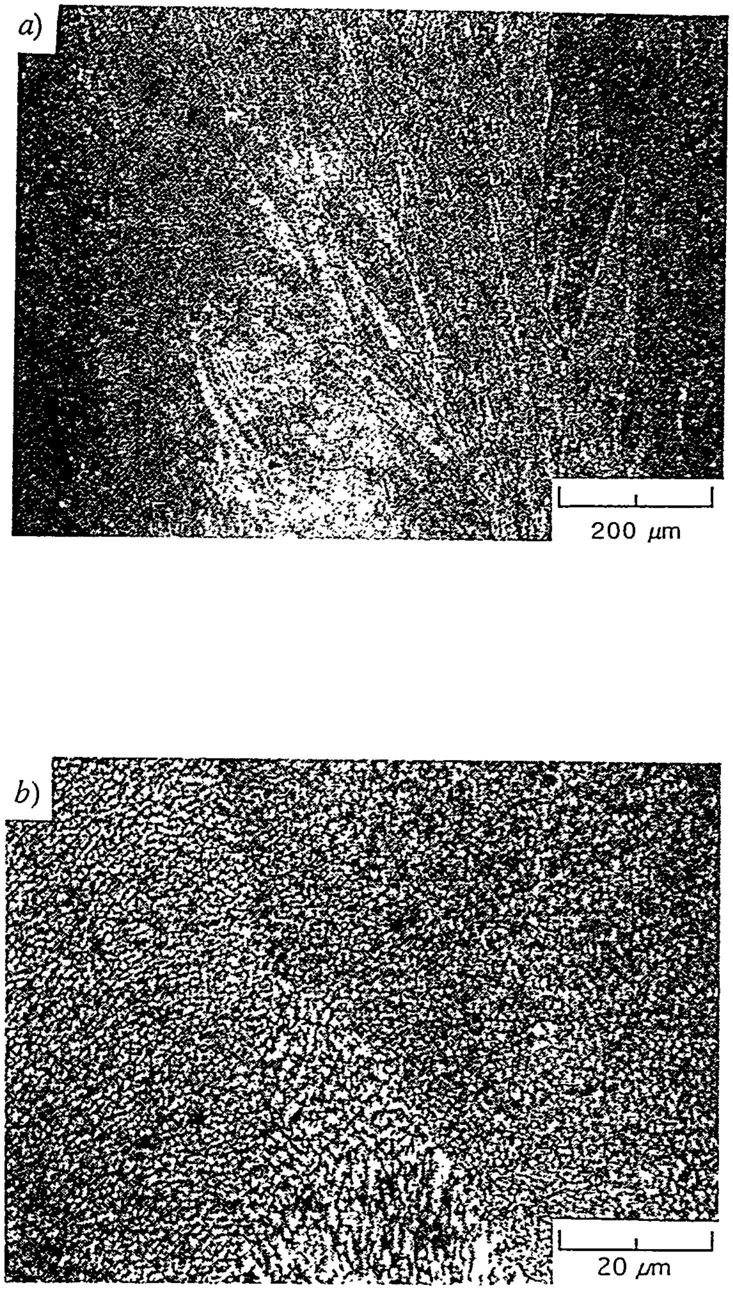

Figure 4.3 Optical micrographs of Sn-4.7Ag-1.7Cu wt% chill cast sample etched with 2 vol % HCl in methanol. *a*) eutectic colonies at low magnification, *b*) high magnification of *a*).

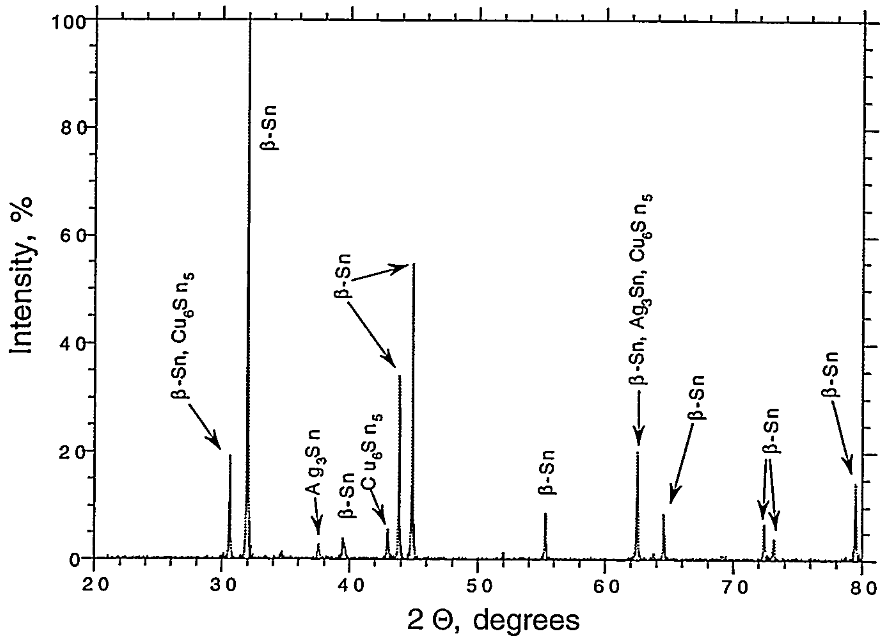

***Figure* 4.4** Diffraction pattern of Sn-4.7Ag-1.7Cu wt% alloy (bulk sample).

It should be pointed out that the melting temperatures obtained with DTA varied systematically depending on the form of the calibration sample: solid or powder. Initial calibration of the DTA apparatus was done with solid bulk samples of both pure Sn and Zn. The measured onset of melting of the Sn-4.7Ag-1.7Cu wt% powder sample was 216.5 °C. Before performing DTA on the PDM samples, the apparatus was calibrated to powder Sn and solid bulk Zn samples. The recorded onset of melting for the powder Sn-4.7Ag-1.7Cu wt% sample with this calibration was 217.5 °C, 1.0 °C above the previously measured onset of melting. Although this discrepancy is small (< 0.5%) it was noticeable since the measured melting temperatures were very consistent from sample to sample. It has been shown that sample size does have an effect on the temperature at which a thermal event occurs for a given material (48). Therefore, a melting temperature of 217.0 ± 0.5 °C is believed to be the more accurate ternary eutectic melting temperature since the calibration sample, Sn, was in the same powder form compared to the powder PDM samples.

The liquidus temperatures of samples 1, 6 and 7 were seen as secondary endothermic peaks separate from the initial onset of melting, Figures A1, A6 and A7. The liquidus temperatures of the remaining samples were difficult to read on the DTA thermogram since the liquidus peak overlapped with the initial onset of melting, or solidus peak. However, by visually examining the curvature of the positive slope side of the main peak a slight saddle point could be seen. This saddle point was caused by a thermal event corresponding to the liquidus temperature.

Of most interest, however, is the fact that the melting temperature of the Sn-4.7Ag-1.7Cu wt% sample is 217 ± 0.5 °C which is 4 °C lower than the Sn-Ag eutectic temperature of 221 °C, the lowest binary eutectic melting temperature of the ternary system. This ternary eutectic melting temperature is also 8 °C lower than the previously published four-phase equilibrium temperature of 225 °C.

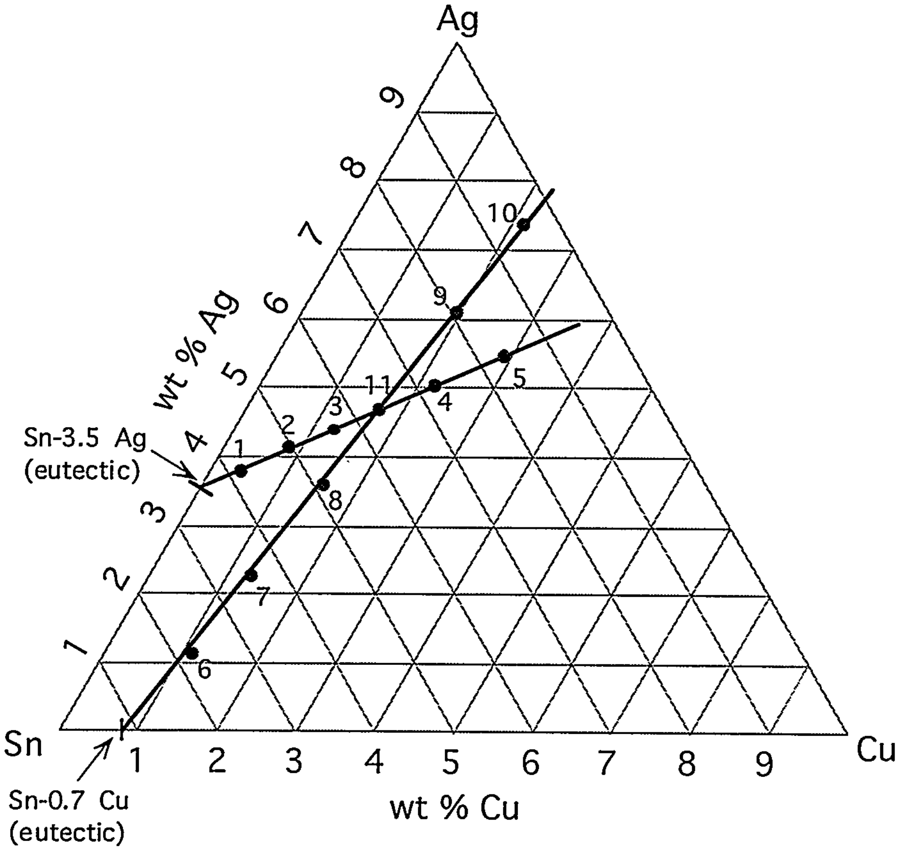

Figure **4.5** Composition of cast samples for phase diagram mapping.

Table 4.1 Composition of samples cast for phase diagram determination.

Sample #	wt% Sn	wt% Ag	wt % Cu
PDM1	95.80	3.80	0.40
PDM2	95.00	4.10	0.90
PDM3	94.30	4.40	1.30
PDM4	92.90	5.00	2.10
PDM5	91.70	5.50	2.80
PDM6	97.80	1.10	1.10
PDM7	96.40	2.30	1.30
PDM8	94.90	3.60	1.50
PDM9	92.00	6.10	1.90
PDM10	90.50	7.40	2.10
PDM11	93.60	4.70	1.70

Table 4.2 Summary of DTA results.

Sample	Solidus Temperature, °C	Liquidus Temperature, °C	Δ T, °C
PDM1	216.7	218.9	2.2
PDM2	217.3	218.0	0.7
PDM3	217.3	218.3	1.0
PDM4	217.4	218.3	0.9
PDM5	217.1	218.0	0.9
PDM6	217.2	223.7	6.5
PDM7	217.4	220.6	3.2
PDM8	217.2	218.3	0.9
PDM9	217.3	218.3	1.0
PDM10	217.3	217.9	0.6
PDM11	217.5	--	0.0

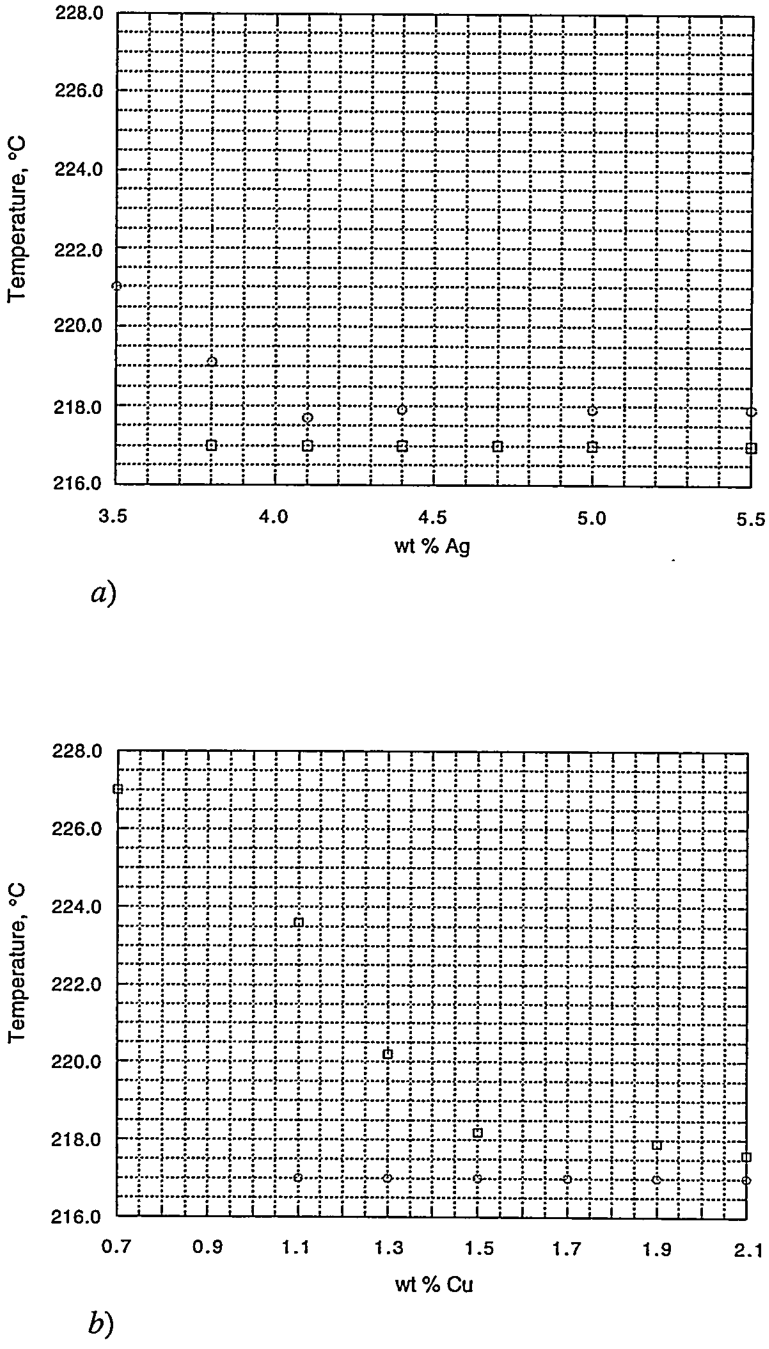

Figure 4.6 Isopleth from *a*) Sn-Ag and *b*) Sn-Cu binary eutectics through the proposed Sn-4.7Ag-1.7Cu wt% ternary eutectic composition.

4.2. Casting Conditions

When casting alloy samples by melting the constituent elements together, it is likely that the elements themselves have different melting temperatures. Therefore, it is important to be sure that all of the elements become completely dissolved in the melt. In the case of a Sn-Ag-Cu alloy, if one element does not completely melt this could effect the resulting microstructure of the cast sample since the molten liquid composition is not what it is desired to be. To examine this for the Sn-Cu-Ag system, several alloys were cast (designated SHx for super heat) at different superheats and held at the superheat temperature for various times. Their microstructure was examined using optical and scanning electron microscopy to look for incomplete melting or dissolution of the original elements. Parameters for the different superheats are given in Table 4.3.

Table 4.3 Times and temperatures of superheat samples.

Sample	Time	Temperature, °C
SH1	16 h	500
SH2	45 min	500
SH3	45 min	650
SH4	45 min	300

Optical and SEM micrographs taken of the super heat samples are shown in Figures 4.7 and 4.8. The regions examined all were located on the end of the chill cast ingots (see Figure 3.2). The scanning electron micrographs show the eutectic microstructure whereas the optical micrographs give an overall view of the microstructure. In the samples heated for short times and lower temperatures (SH2 and SH4) it can be seen that the microstructure contains many large intermetallics. The samples heated for high temperatures and long times (SH1 and SH4) show a more homogeneous microstructure. The sample which was only heated for 45 min at 300 °C clearly shows undissolved solid Cu (see Figure 4.9). This would

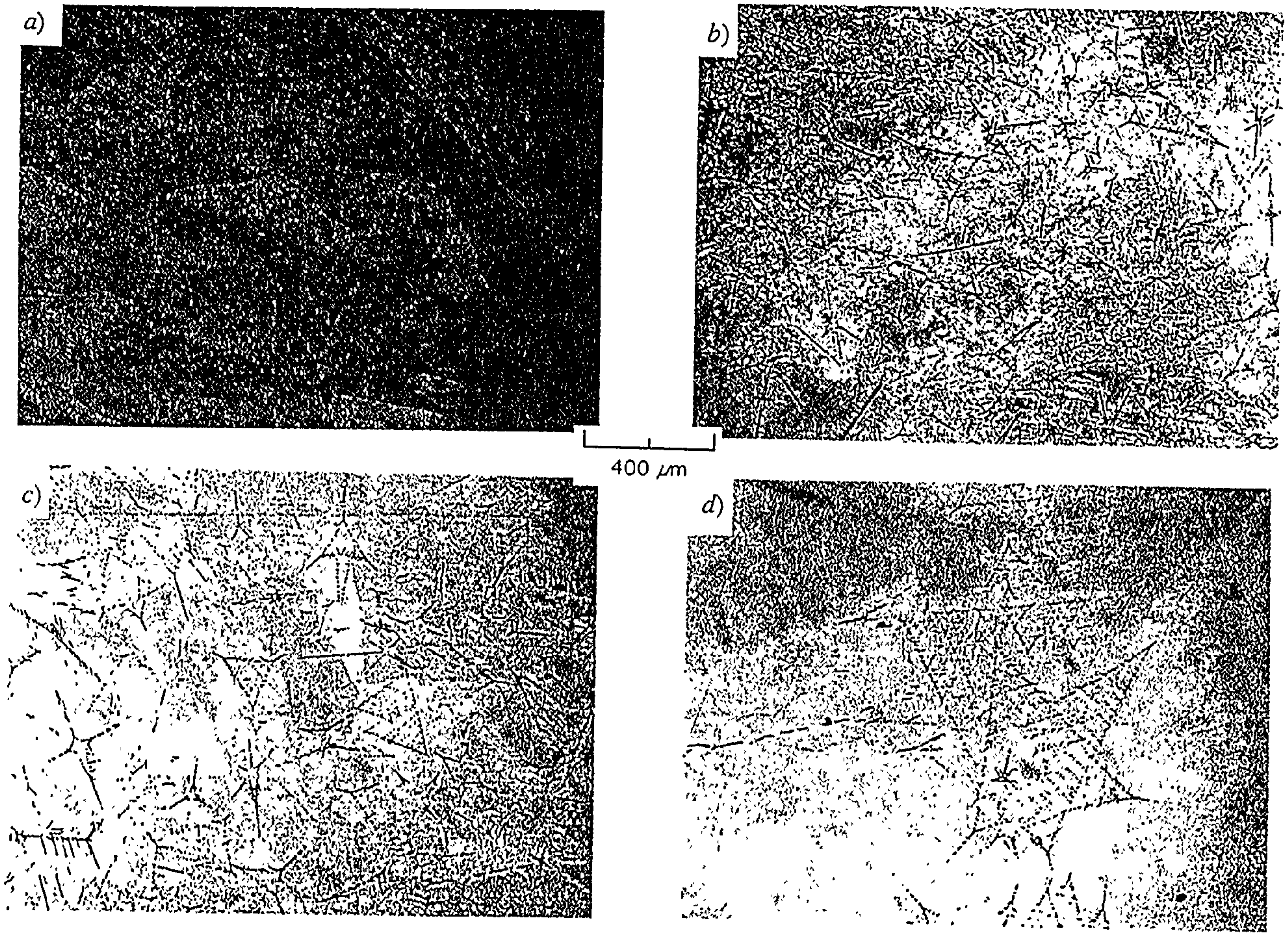

Figure 4.7 Optical micrographs of Sn-4.7Ag-1.7Cu wt% chill cast samples etched with 2 vol % HCl in methanol. Casting parameters *a*) 300 °C, 45 min, *b*) 500 °C, 45 min *c*) 500 °C, 16 hours and *d*) 650 °C, 45 min.

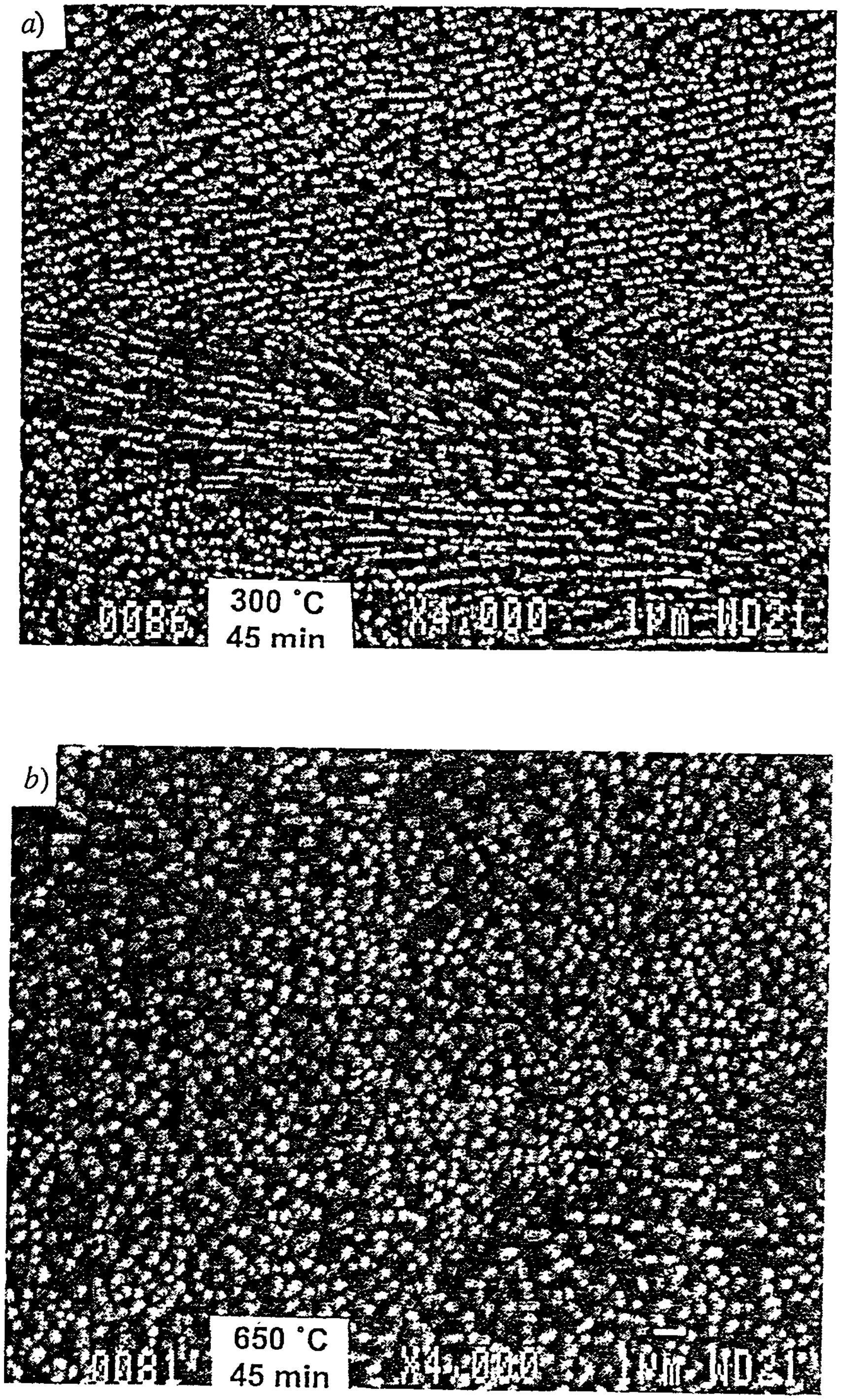

Figure 4.8 SEM micrographs (secondary electron) of Sn-4.7Ag-1.7Cu wt% chill cast sample at *a*) 300 ˚C for 45 min and *b*) 650 ˚C for 45 min. Dark contrast *β*-Sn penetrated by light intermetallic phase.

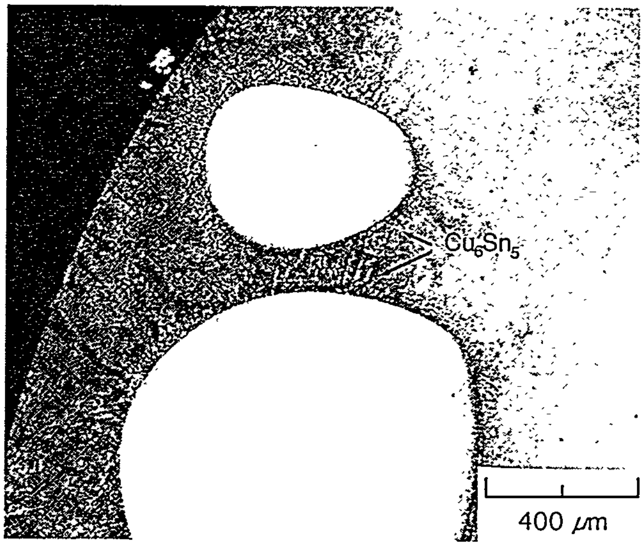

Figure 4.9 Optical micrograph of Sn-4.7Ag-1.7Cu wt% chill cast sample unetched. The light contrast circles are undissolved Cu. The arrows point to the Cu_6Sn_5 intermetallic layer on the pure Cu.

indicate that either the time was too short or the temperature too low (probably both are the case) for sufficient diffusion of Cu to occur into the Sn-rich alloy liquid.

4.3. Cooling Rate Study

To investigate the effect of cooling rate on the microstructure of the ternary eutectic solder, 120 mg solder samples were cooled on small Cu blocks (see Figure 4.10) from 250 °C to 25 °C at rates varying from 0.2 to almost 200 °C/sec. A diagram of the experimental setup is shown in Figure 4.11. Table 4.4 relates the method of cooling to the corresponding cooling rate and a plot of the cooling rates is shown in Figure 4.12. The surface of each Cu block was prepared immediately before use by grinding with 600 grit SiC paper and rinsing thoroughly with isopropyl alcohol. For each run, a thermocouple was attached to the Cu block with a nut and screw. The Cu block was then placed on a hot plate which was at ≈ 260 °C and the temperature and time were recorded with a computer (see Figure 4.12). As each Cu block was heated, drops of RMA flux was placed on it using a small syringe with a needle. When the temperature of the block reached about 170 °C a 120 mg piece of Sn-4.7Ag-1.7Cu wt% alloy was placed on the block, followed by more flux. When the temperature of the block reached 250 °C, the block was cooled at the specified rate. Two solder samples were cooled at each rate.

Each sample was sectioned along the longitudinal axis such that two surfaces could be examined. Therefore, for each cooling rate a mount was made which contained four surfaces. The samples were examined metallographically using both optical and scanning electron microscopy, looking for differences in eutectic spacing and the size and dispersion of the intermetallics present. The hardness of the eutectic matrix was also measured using the Vickers microhardness test.

Scanning electron micrographs taken of the solder samples cooled at different rates are shown in Figures 4.13 and 4.14. It can be seen that the presence of large intermetallic

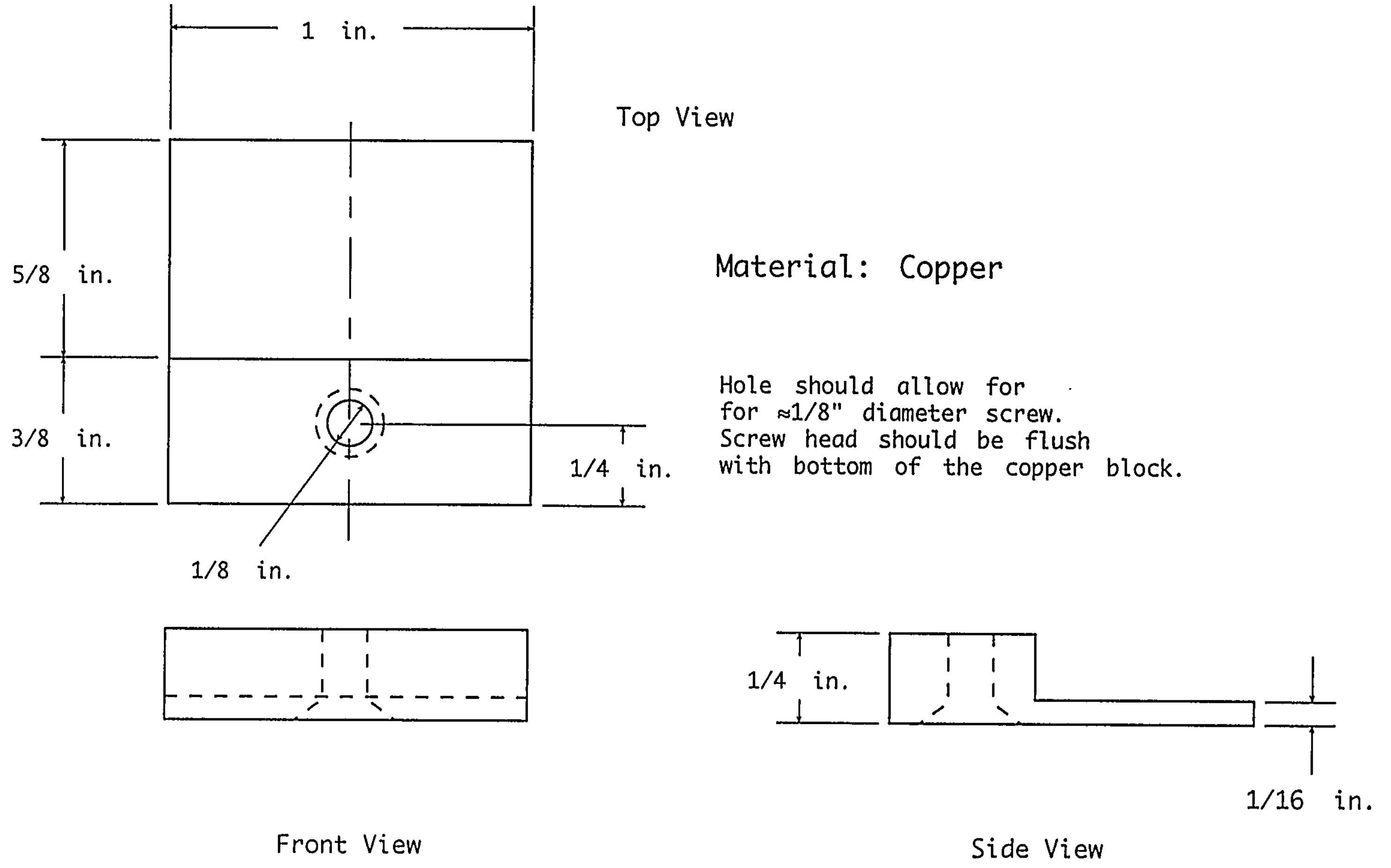

Figure **4.10** Specifications for Cu block used in cooling rate study.

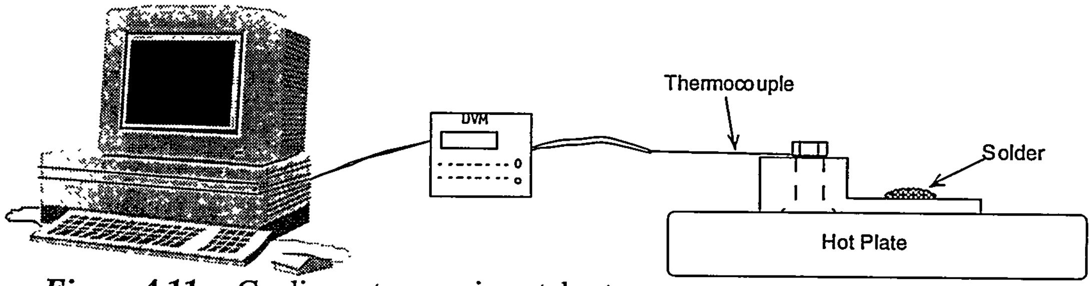

Figure **4.11** Cooling rate experimental setup.

Table 4.4 Cooling rates obtained for various methods of cooling.

Method of Cooling	Cooling Rate, °C/sec
Hot plate turned off, sample remained on hot plate.	0.2
Sample placed on ceramic brick.	0.8
Sample placed on ceramic brick under forced air convection.	1.8
Sample placed on large 61.75 in^3 Cu block.	8.9
Sample quenched in 20°C water.	2.0×10^2

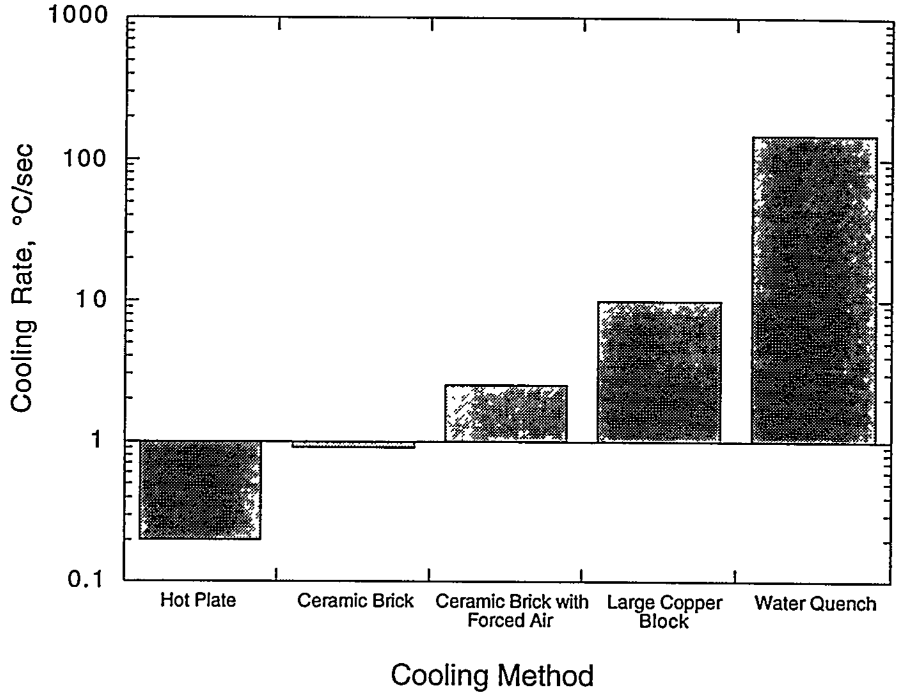

Figure **4.12** Cooling rates obtained for different cooling methods.

particles distributed within the eutectic phase of the bulk solder decreases with increasing cooling rate. Also, the distribution of the intermetallics becomes more localized to the Cu/solder interface with increasing cooling rate. Coarse intermetallic formation appears to be constrained to an area close to the Cu substrate at higher cooling rates and, ultimately, no significant coarse intermetallic formation occurs in the bulk solder at the fastest cooling rate of 150 °C (see Figure 4.13*d*).

The hardness of the samples are shown in Figure 4.15. This shows a direct correlation between cooling rate and hardness. Ideally, since higher hardness corresponds to higher strength, a fast cooling rate is desired.

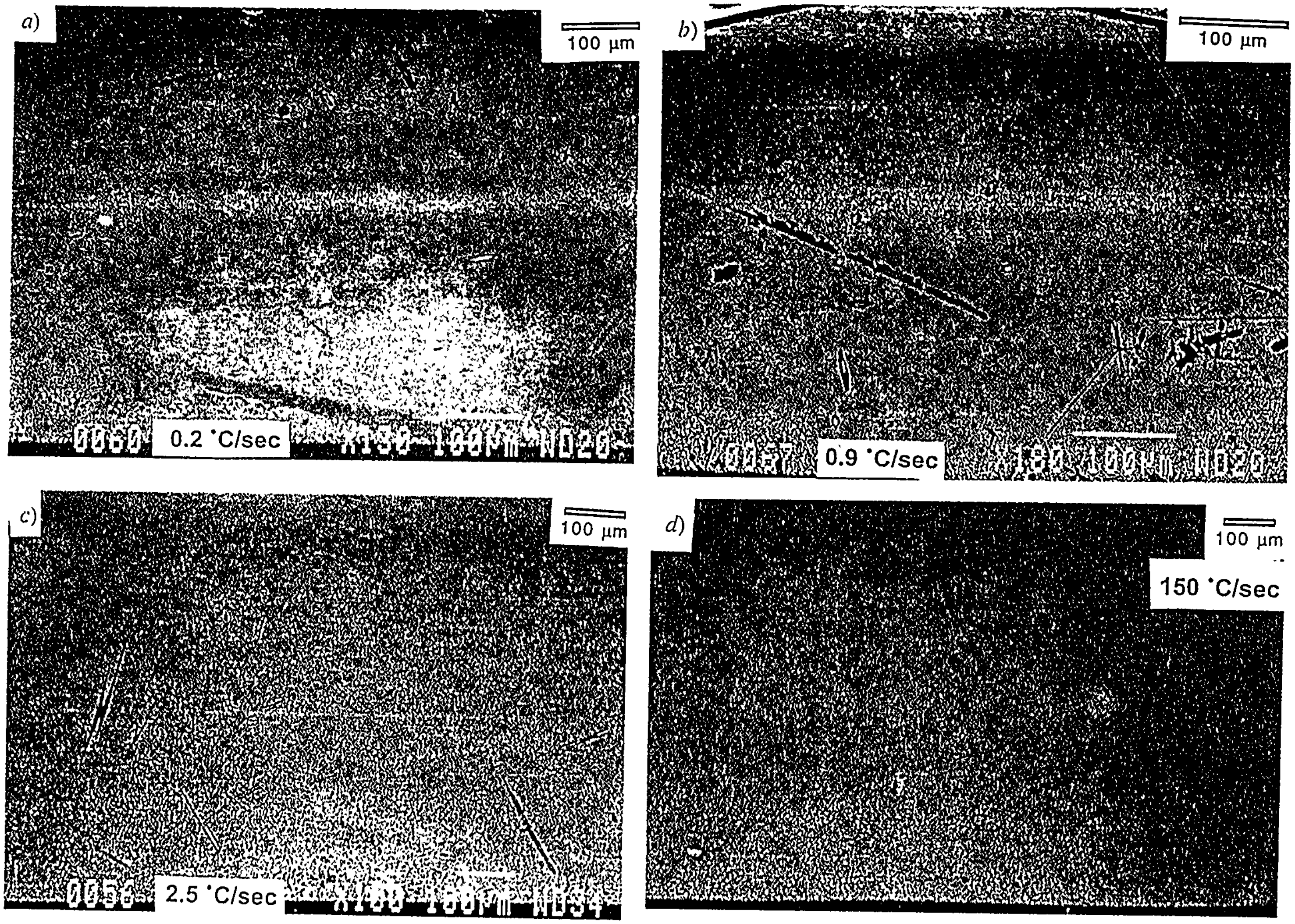

Figure 4.13 SEM micrographs (secondary electron) of Sn-4.7Ag-1.7Cu wt% chill cast sample lightly etched with 2 vol % HCl in methanol. Cooled at *a*) 0.2 ˚C/sec, *b*) 0.9 ˚C/sec, *c*) 2.5 ˚C/sec and *d*) 150 ˚C/sec. Dark phase at bottom of each micrograph is pure Cu, growth direction is up.

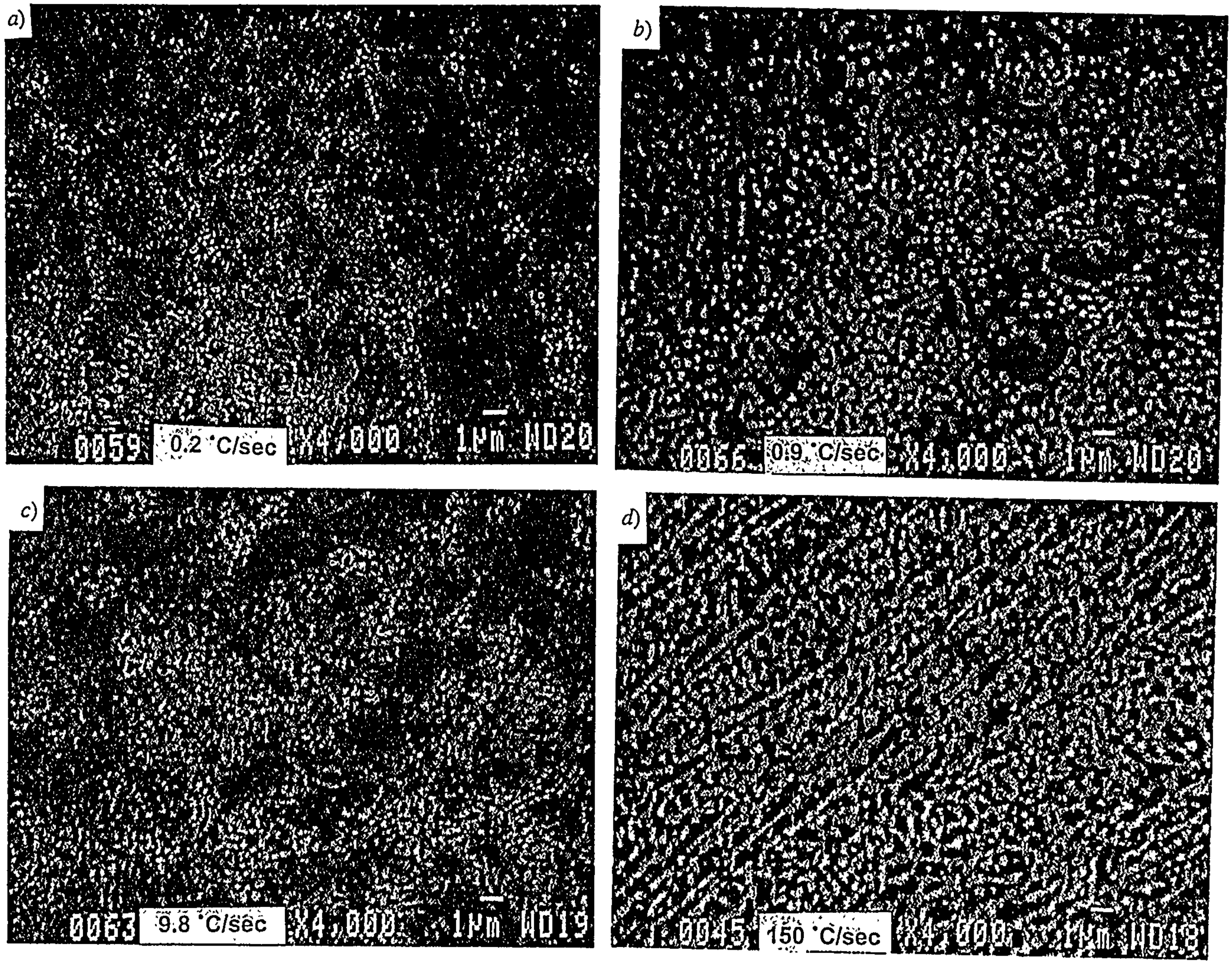

Figure 4.14 SEM micrographs (secondary electron) of Sn-4.7Ag-1.7Cu wt% chill cast sample lightly etched with 2 vol % HCl in methanol. Cooled at *a*) 0.2 °C/sec, *b*) 0.9 °C/sec, *c*) 2.5 °C/sec and *d*) 150 °C/sec. Micrographs show eutectic microstructure at high magnification.

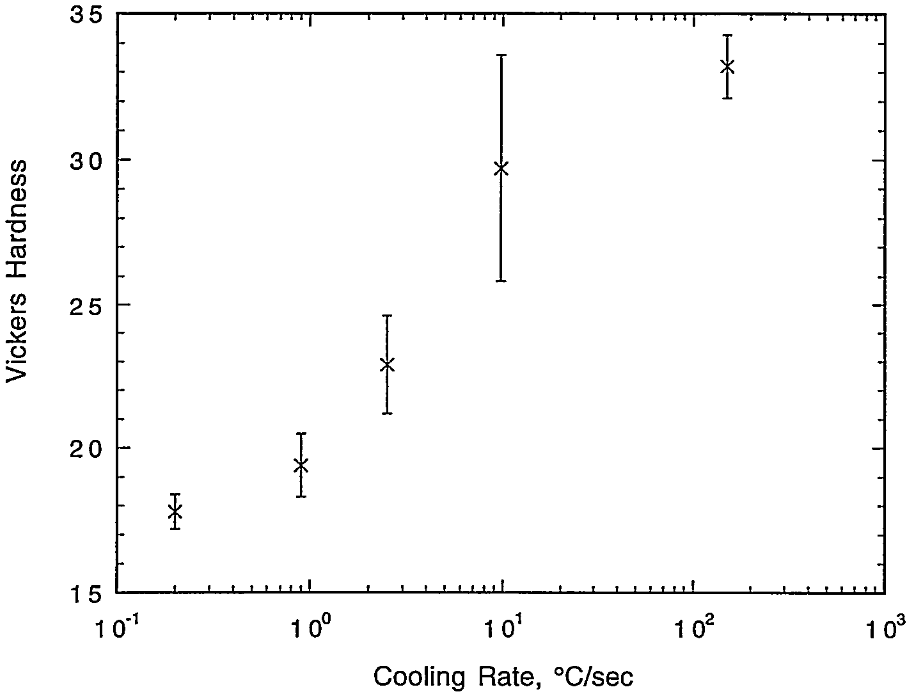

***Figure* 4.15** Hardness vs. cooling rate for Sn-4.7Ag-1.7Cu wt% alloy.

4.4. Microstructural Stability

One hundred hand solder joints were made on a test circuit board by an Ames Lab electronics technician. A standard RMA flux was used as surface preparation on the board. The joints consisted of Cu wire soldered into the Cu grommets of the circuit board.

The solder joints were diamond saw cut out of the circuit board in pairs, heat treated for various times and temperatures, mounted and microstructurally analyzed in an SEM and tested for microhardness. Annealing temperatures ranged from 130 to 210 °C by increments of 20 °C. The annealing times ranged from 10^3 to 10^6 seconds by increments of half an order of magnitude. Hardness samples were mounted in cross section and SEM samples were mounted traversely, as given in Figure 4.16.

The SEM pictures obtained from the different samples were digitally analyzed for area percent and average size of the intermetallic particles using the computer program NIH Image 1.55 for the Macintosh.

Visual inspection of the SEM micrographs of solder joints before and after annealing indicates that the Cu_6Sn_5 and Ag_3Sn intermetallic phases do indeed coarsen, Figures 4.17-4.19. All photomicrographs were shot at the same magnification. The coarsening results in a more rounded morphology. Results of the areal analysis of Cu_6Sn_5 phase performed on the SEM micrographs is given in Table 4.5.

Hardness measurements taken on the sample indicate that the alloy retains nearly 60% of its hardness even after severe annealing at a homologous temperature of 0.98 (see Figure 4.20). This is an indication that the alloy will maintain most of its initial strength even when used in high temperature applications.

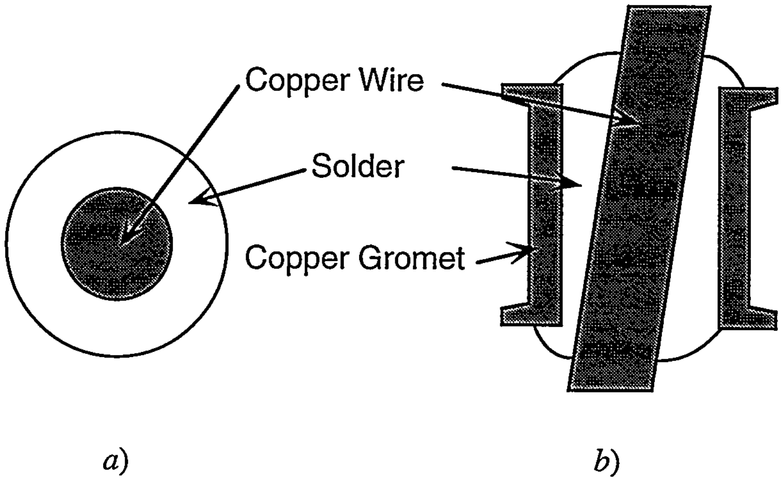

***Figure* 4.16** Mounted solder joint samples.

Table 4.5 Summary of areal analysis of Cu_6Sn_5 in annealed samples.

Variable Held Constant	Anneal	Area %	Average Particle Area	Particle Aspect Ratio
t=5000 sec	No anneal	2.2	16.5	1.8
	130 °C	2.6	16.0	1.9
	170 °C	2.6	10.6	1.8
	210 °C	4.3	11.4	1.8
t=500,000 sec	No anneal	2.2	16.5	1.8
	130 °C	4.2	26.1	2.2
	170 °C	4.9	26.2	2.2
	210 °C	6.1	83.2	2.2
T=170 °C	No anneal	2.2	16.5	1.8
	5000 sec	2.6	10.6	1.8
	500,000 sec	4.9	26.2	2.2

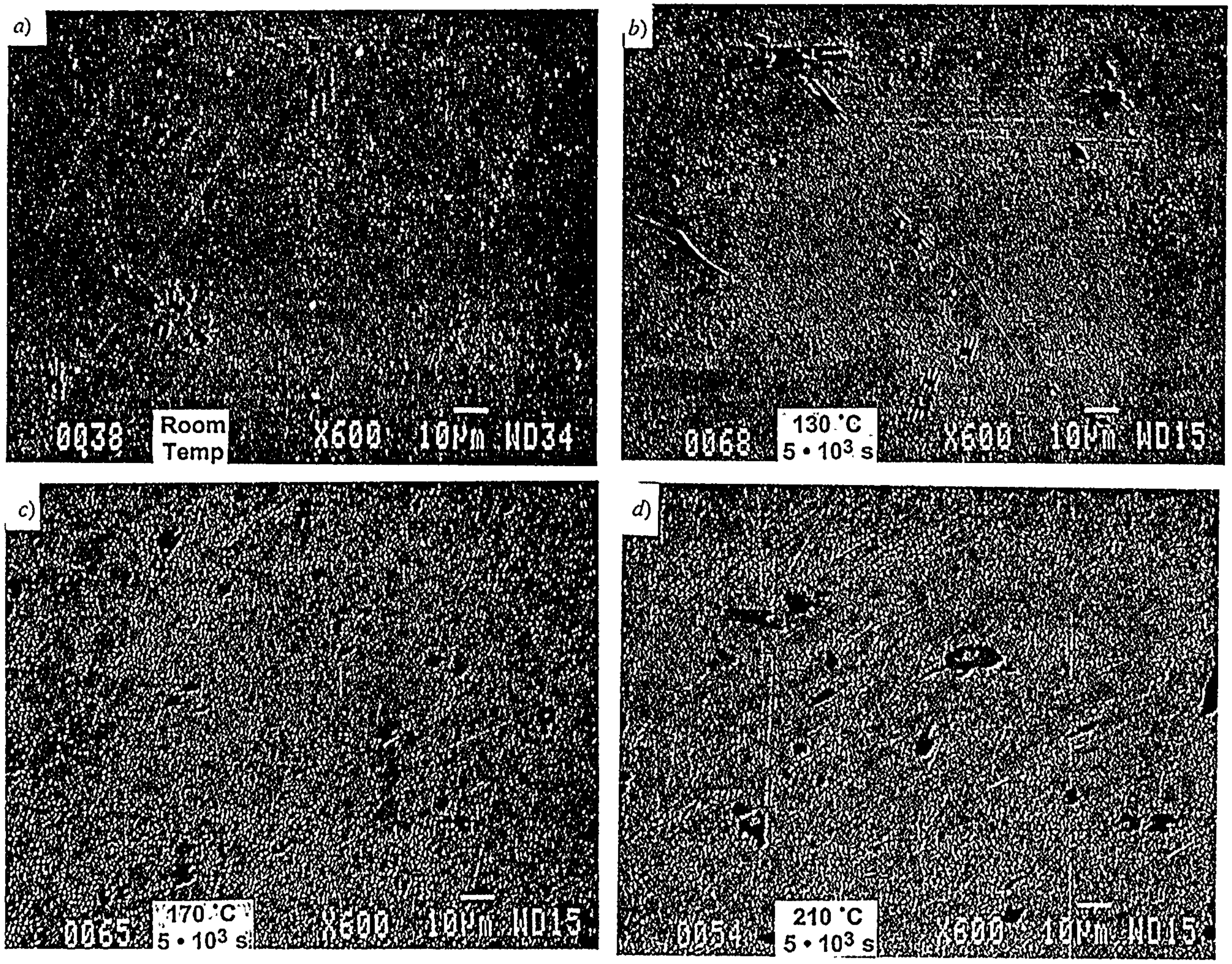

Figure 4.17 SEM micrographs (secondary electron) of Sn-4.7Ag-1.7Cu wt% chill cast sample lightly etched with 2 vol % HCl in methanol. Dark contrast Cu_6Sn_5 phase coarsened out of ternary eutectic. Samples annealed for *a*) no anneal, *b*) 5000 sec at 130 °C, *c*) 5000 sec at 170 °C and *d*) 5000 sec at 210 °C.

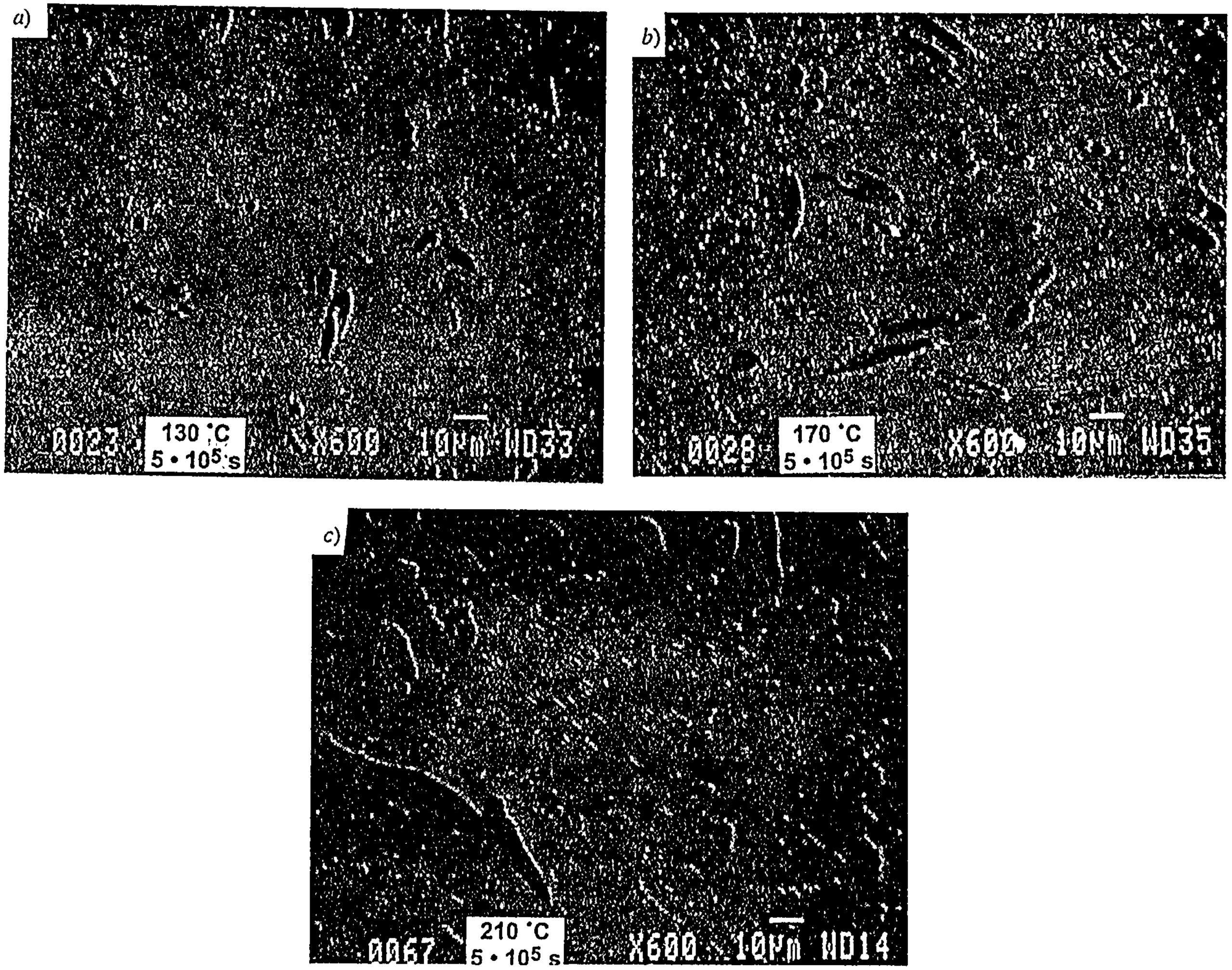

Figure 4.18 SEM micrographs (secondary electron) of Sn-4.7Ag-1.7Cu wt% chill cast sample lightly etched with 2 vol % HCl in methanol. Dark contrast Cu_6Sn_5 phase coarsened out of ternary eutectic. Samples annealed for 500,000 seconds at *a*) 130 °C, *b*) 170 °C and *c*) 210 °C.

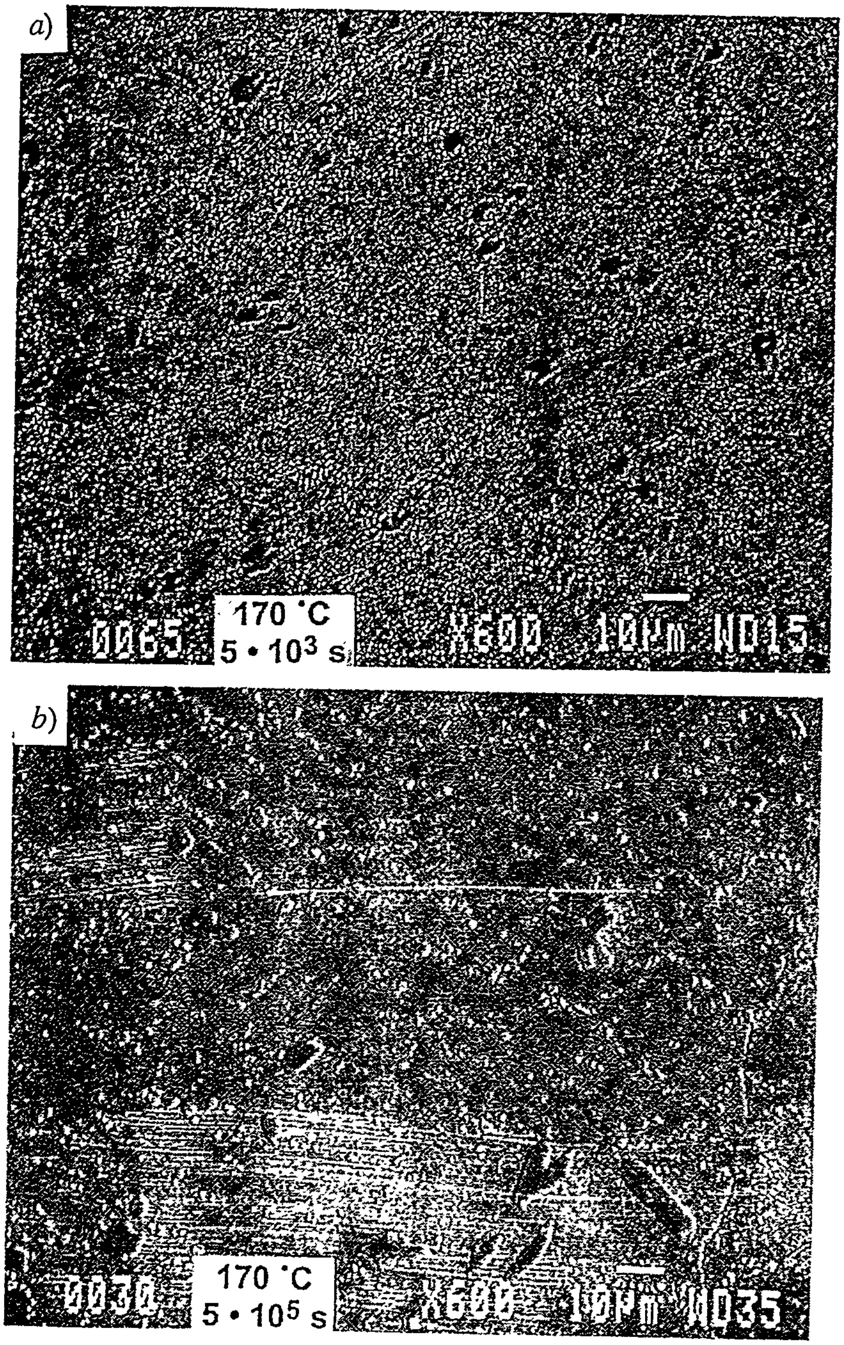

Figure **4.19** SEM micrographs (secondary electron) of Sn-4.7Ag-1.7Cu wt% chill cast sample lightly etched with 2 vol % HCl in methanol. Dark contrast Cu_6Sn_5 phase coarsened out of ternary eutectic. *a*) Annealed 5000 sec at 170 °C, *b*) annealed 500,000 sec at 170 °C.

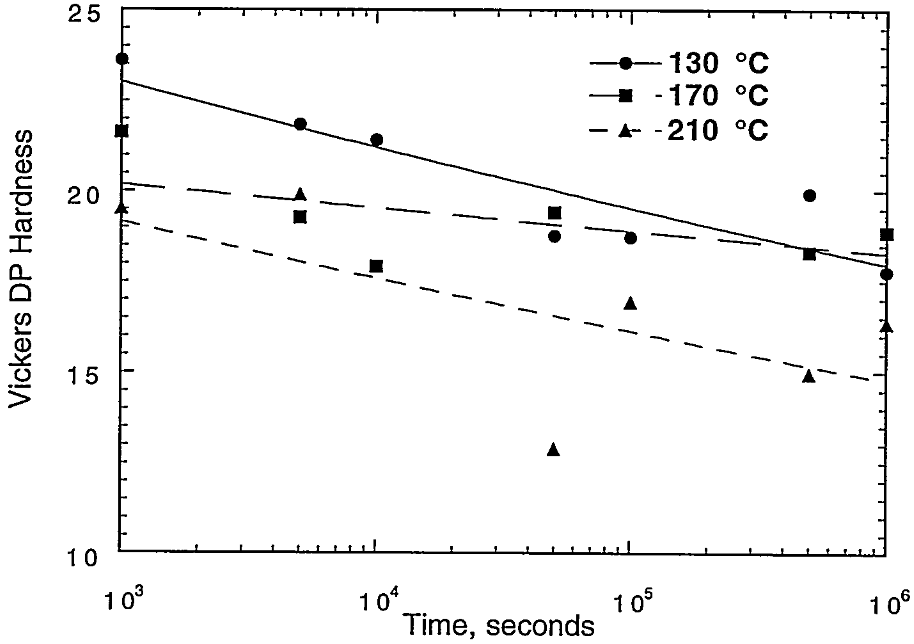

***Figure* 4.20** Summary of Vickers microhardness vs. different annealing schedules for the Sn-4.7Ag-1.7Cu wt% eutectic alloy.

5. DISCUSSION

5.1. Phase Diagram Determination

Microscopic inspection of as cast Sn-4.7Ag-1.7Cu wt% and Sn-3.6Ag-1.5Cu wt% samples revealed a eutectic microstructure in both. However, the Sn-3.6Ag-1.5Cu wt% sample contained a fair amount of β-Sn dendritic growth (see Figure 4.1). Since the cooling rates (and, therefore, presumably the solidification rates) of the two samples were essentially the same, the vast variation in microstructure is probably a direct result of the difference in alloy composition and the corresponding alloy constitution differences.

The microprobe, or WDS, analysis proved invaluable in providing the quantitative composition of the eutectic microstructure. Taking the standard deviation of the data into account, as indicated in Figure 4.2, the averaged eutectic composition, Sn-4.7Ag-1.7Cu wt%, is probably close to the exact ternary eutectic composition. The composition deviation from run to run can be attributed primarily to inherent shortcomings of the microprobe electron beam "spot." The electron beam interacts not only with the surface of the sample but with a tear-shaped interaction volume below the surface. Hence, if a coarse intermetallic, such as Cu_6Sn_5 or Ag_3Sn, happened to be immediately beneath a polished surface that appeared to be a uniform eutectic microstructure, then the resulting microprobe x-ray intensities for Cu or Ag, respectively, would be higher than if the interaction volume contained only eutectic phase. Of course, the relative Sn x-ray intensity would increase if a dendrite arm of β-Sn was just beneath the surface of polish and, therefore, in the interaction volume.

The measured eutectic melting temperature of 217 °C is 8 °C lower than the published four phase equilibrium temperature of 225 °C (44). In addition, 217 °C is lower than the lowest binary eutectic melting temperatures of the system, Sn-3.5Ag at 221 °C and Sn-0.7Cu (wt%) at 227 °C. This supports the hypothesis that the Sn-Ag-Cu system contains a Class I four-phase equilibrium (ternary eutectic) reaction at 217 ± 0.5 °C: $L \Rightarrow \eta + \theta + \beta$-Sn ($L$ = liquid, $\eta = Cu_6Sn_5$, $\theta = Ag_3Sn$). A revised estimate of the Sn-rich corner of the Sn-Ag-Cu system based on these data is given in Figure 5.1. The presence of these 3 phases in the as-solidified microstructure was also confirmed by x-ray analysis (see Figure 4.4). The consistency of the solidus temperatures of the PDM samples in the Sn-rich region indicates that an isothermal plane, which is characteristic of a class I four-phase equilibrium reaction (56), exists in the Sn-Ag-Cu system. This contradicts the previously published (44) class II four-phase equilibrium reaction at 225 °C: $L + \eta \Rightarrow \theta + \beta$-Sn. In addition, the measured melting temperature of 217 °C is in agreement with recent phase diagram calculations performed by Kattner (57) who reported a ternary eutectic melting temperature of 217.4 °C for this system.

The results of DTA, microprobe and microscopy were supported by x-ray analysis. In an x-ray diffraction pattern obtained from a Sn-4.7Ag-1.7Cu wt% alloy, every phase present within the eutectic microstructure (Cu_6Sn_5, Ag_3Sn, β-Sn) was indexed to a diffraction peak (see Figure 4.4). The x-ray sample was an as cast solid sample whose microstructure matched that of Figure 4.3. Therefore, the phases which were indexed were most likely present in a refined eutectic microstructure and not in the form of coarsened intermetallics.

In determining the Sn-Ag-Cu phase diagram, very sensitive DTA measurements were used. However, even with this sensitive technique there remain ambiguities in the data. Samples which were furthermost from the ternary eutectic composition contained at least two distinct endothermic peaks and in these cases the liquidus temperature could easily be obtained, e.g., Figures A1, A6 and A7 of the Appendix, as the final endothermic peak. For most of the samples, however, the solidus and liquidus endothermic peaks appeared to overlap. In order to read the liquidus temperatures, the DTA thermograms were carefully examined by eye. The liquidus temperature was identified as the last inflection point on the composite endothermic curve, i.e., the final melting event.

The DTA data obtained were plotted as isopleths extending from the binary eutectic compositions through the proposed ternary eutectic composition (see Figure 4.6). On these plots, an estimate of the liquidus curve for each isopleth was drawn (see Figures 5.2*a*, *b*). Such an estimate is useful for improving the calculation of this phase diagram. However, for a full mapping of the ternary liquidus surfaces in the Sn-rich corner of the Sn-Ag-Cu system, additional data are needed.

The liquidus curve on each isopleth is easily seen on solute poor samples (to the left of the proposed ternary eutectic composition (see Figure 5.2) . To the right of the eutectic composition the liquidus curve a trend is difficult to identify. This could be a result of several factors. The distances from the ternary eutectic composition to the binary eutectic compositions are very short when compared to the distance from the ternary eutectic to the intermetallic phase boundaries. Hence, the slopes of these liquidus surfaces from the binary eutectics towards the ternary eutectic are large. From the ternary eutectic composition towards the intermetallic phase boundaries, the liquidus surfaces are much more extended with lower slopes. This could account for the apparent lack of a strong trend for each rising liquidus curve on the right side of the eutectic composition (see Figure 5.2).

Another source for error might have been in the selection of isopleths to analyze. It is possible that the estimated eutectic composition of Sn-4.7Ag-1.7Cu wt% is not exactly correct. Also, the actual liquidus troughs extending from the binary eutectics to the ternary eutectic may not be precisely straight. Figure 5.3 shows three different cases for how an actual liquidus trough might appear as compared to an experimental isopleth. The simplest situation, case 1, shown in Figure 5.3*a*, illustrates that the actual liquidus trough and experimental isopleth lie on the same line. Case 2, shown in Figure 5.3*b*, shows that even

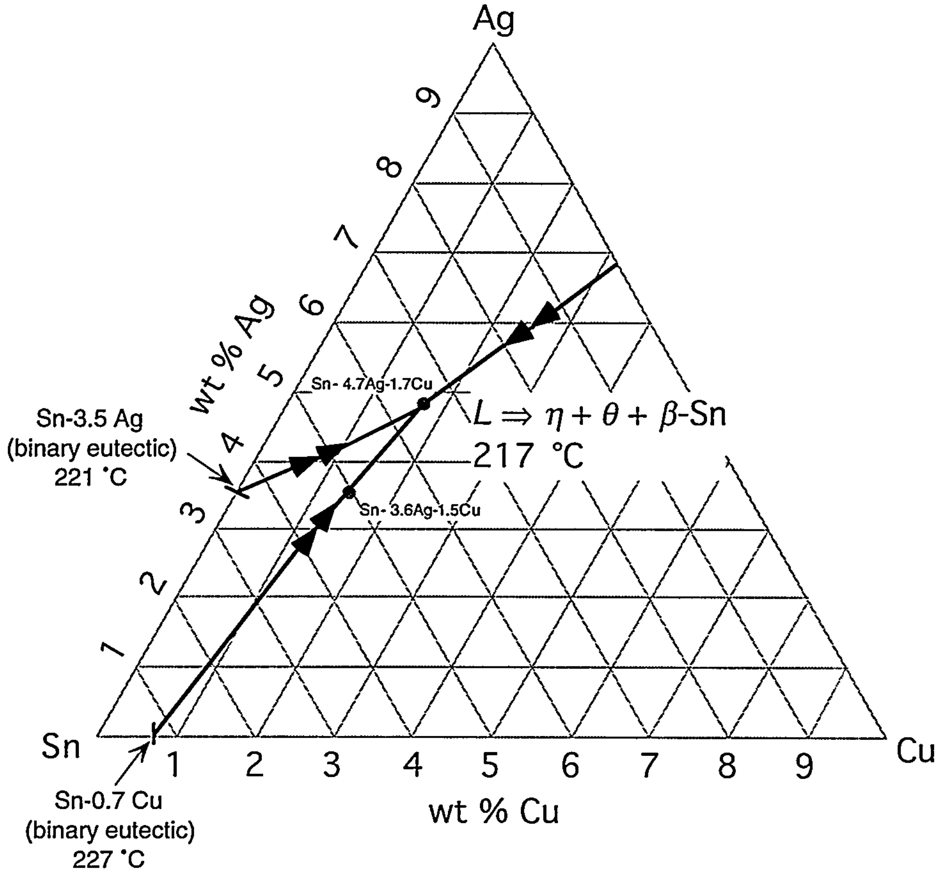

***Figure* 5.1** Revised estimate of Sn-rich region of Sn-Ag-Cu phase diagram.

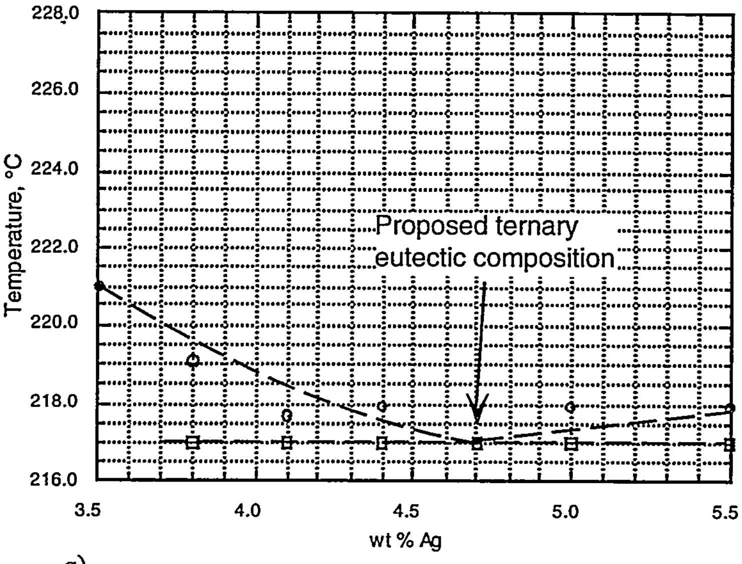

a)

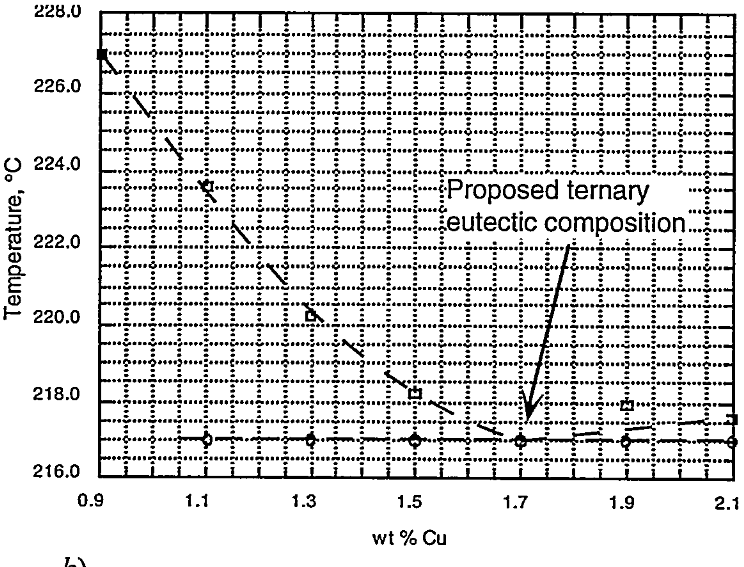

b)

Figure 5.2 Estimated liquidus curves on two selected isopleth sections of the Sn-Ag-Cu system *a*) Sn-Ag eutectic towards Sn-4.7Ag-1.7Cu wt% and *b*) Sn-Cu eutectic towards Sn-4.7Ag-1.7Cu wt%.

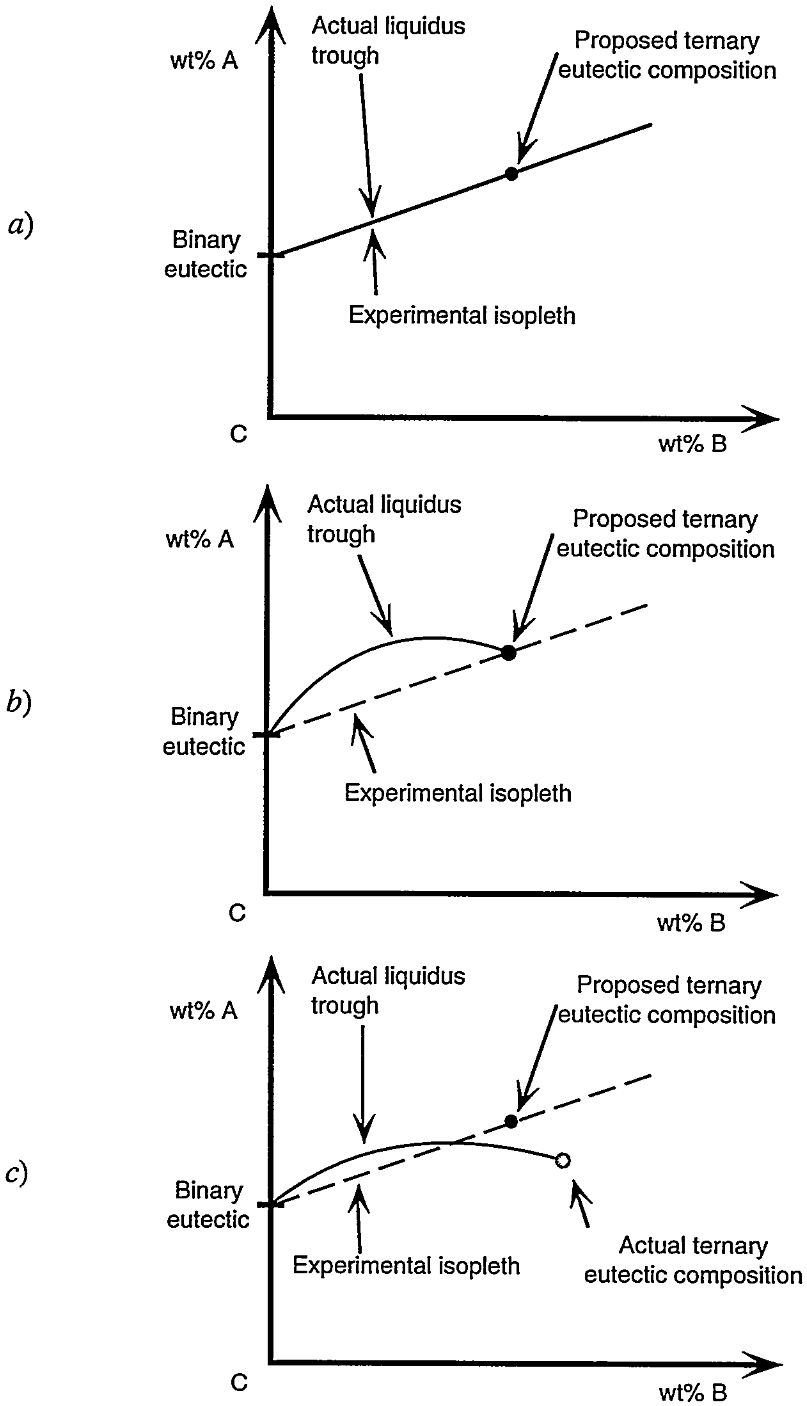

***Figure* 5.3** Liquidus projections showing possible liquidus paths: *a*) actual liquidus trough matches experimental isopleth, *b*) proposed ternary eutectic matches actual ternary eutectic and *c*) experimental isopleth passes through liquidus through (two liquidus surfaces).

though the proposed ternary eutectic composition equals the actual ternary eutectic composition the experimental isopleth doesn't follow the actual liquidus trough. A third possibility, case 3, Figure 5.3*c*, shows that the experimental isopleth may cross two liquidus surfaces if both the true curvature of the trough and the actual ternary eutectic composition do not match the isopleth and the proposed ternary eutectic composition, respectively.

Specifically, the isopleth which was chosen from the Sn-Ag binary towards the ternary eutectic could have actually crossed two different liquidus surfaces, as in case 3 (see Figure 5.3*c*). Ultimately this may produce confusing DTA data. When the data are plotted as an isopleth, as in Figure 5.3, the measured liquidus temperatures would not have a continuous falling slope leading to the proposed ternary eutectic but rather rise after crossing the trough. This could be the case in Figure 5.2*b*. In hindsight, it would have better to choose at least one additional isopleth which wouldn't lie so close to an actual liquidus trough. Figure 5.4 shows two suggested isopleths which could be studied. This would assist in confirming trends in the melting behavior of the Sn-4.7Ag-1.7Cu wt% alloy.

5.2. Casting Conditions

The casting temperature and the time at which the solder alloy constituents are held at that temperature are important from a manufacturing perspective. The Sn-4.7Ag-1.7Cu wt% alloy contains elements of varying melting temperatures. When cast at a sufficiently high temperature, the higher melting elements of Cu and Ag will dissolve readily in the liquid Sn by a solid to liquid diffusion process. The desired casting process should be feasible in an industrial setting, i.e., a reasonably short time at a reasonably low temperature. This study examined several casting parameters (see Table 4.3).

The sample which was cast at 300 °C for 45 minutes contained relatively large amounts of undissolved Cu in the ingot. Undissolved Ag could not be found but this does not mean that there was no undissolved Ag present. However, when examining the

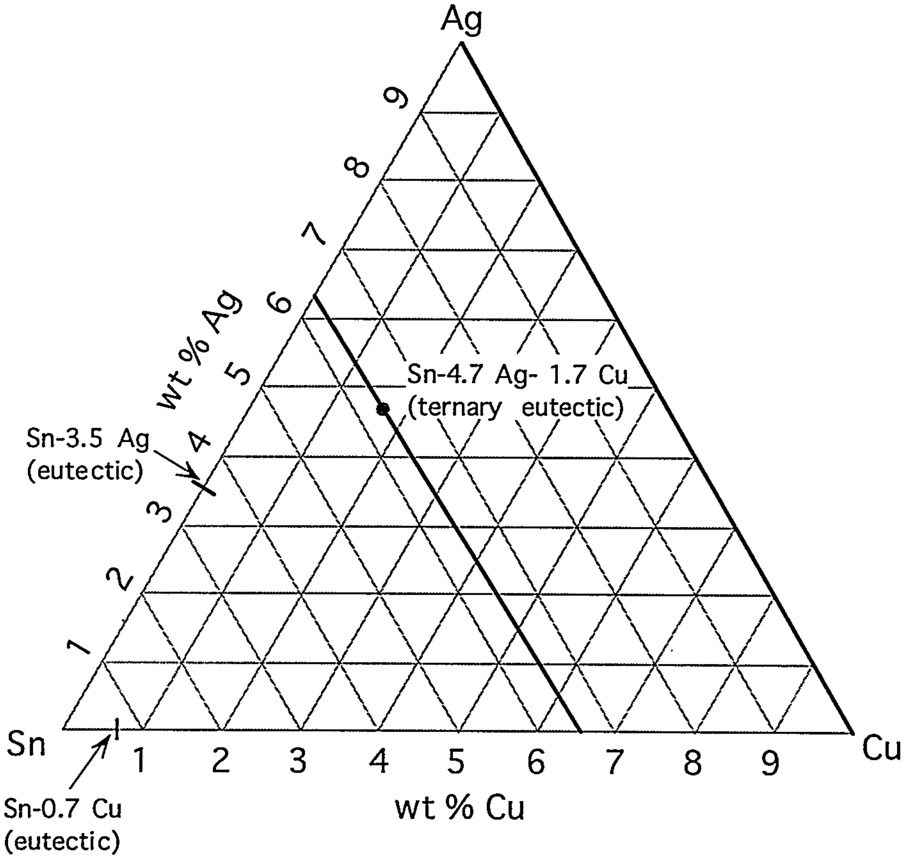

***Figure* 5.4** Ternary diagram. Dark lines show isopleths suggested for future DTA work.

microstructure of the alloy cast at 300 °C for 45 minutes in Figure 4.8*a* it can be seen that the morphologies of the Ag_3Sn intermetallic phase (light contrast) and the β-Sn matrix phase (dark contrast) are elongated. This morphology is typical of the lamellar two-phase eutectic of the Sn-Ag system (43) therefore, a significant amount of Ag has dissolved into the alloy. The microstructure of the alloy cast at 650 °C for 45 minutes in Figure 4.8*b* reveals a microstructure which contains a finely dispersed Ag_3Sn phase (light contrast). The rounded morphology is probably due to the presence of Cu which could refine the eutectic in a way similar to Zn (43). Hence, the 300 °C/45 minute sample has an insufficient amount of Cu dissolved so the Sn-Ag eutectic microstructure remains unrefined with an elongated morphology. The absence of the coarsened Cu_6Sn_5 intermetallic phase in the 300 °C/45 of Figure 4.7a also indicates a deficiency of Cu present in the alloy. Although 300 °C is well above the ternary eutectic melting point of 217 °C, when held at this temperature for only 45 minutes, complete homogenization is not achieved.

The diffusion rate for Cu in liquid Sn at 500 °C was calculated using a first order approximation according to Equation 5.1 where x is half the thickness of the solid sample D is the diffusivity and t is time. The Cu pieces used in casting were about 1 cm lengths of 0.75 mm diameter wire. In this case x is 0.037 cm and the diffusivity of Cu in liquid Sn is 11.5×10^5 cm^2/sec (58). Using the above values and Equation 5.1, the time required for complete dissolution of the Cu sample would be on the order of a nanosecond (10^{-9} sec).

$$x = \sqrt{Dt} \qquad (5.1)$$

Obviously, this is not the mechanism controlling Cu dissolution since solid Cu can be seen in the 300 °C/45 minute sample of Figure 4.9. The barrier mechanism inhibiting the dissolution of Cu is perhaps the formation of an intermetallic layer at the Cu/solder interface, as revealed in the micrograph of Figure 4.9.

It is well known that diffusivity in solid metals is a strong function of temperature as shown in Equation 5.2:

$$D = D_o e^{-Q/RT} \tag{5.2}$$

where Q is the activation, D_O is the diffusion coefficient, R is the gas constant and T is the temperature. Therefore, high diffusion rates are promoted by high temperatures, especially at temperatures that approach the melting point. To calculate a first order estimation of a suitable temperature for casting to dissolve the Cu through the Cu_6Sn_5 layer, the hypothetical congruent melting temperature, T_m, of the intermetallic Cu_6Sn_5 phase was calculated from the enthalpy and entropy of fusion (ΔH^f, ΔS^f) using Equation 5.3.

$$\Delta H^f = T_m \Delta S^f \tag{5.3}$$

The enthalpy and entropy of fusion can be calculated with first order rule of mixtures approximations given in Equations 5.4 and 5.5, where x is the mole fraction of the respective element.

$$\Delta H^f = x_{Cu} \Delta H^f_{Cu} + x_{Sn} \Delta H^f_{Sn} \tag{5.4}$$

$$\Delta S^f = x_{Cu} \Delta S^f_{Cu} + x_{Sn} \Delta S^f_{Sn} + x_{Cu} \ln x_{Cu} + x_{Sn} \ln x_{Sn} \tag{5.5}$$

Substituting Equations 5.4 and 5.5 into Equation 5.3 and solving for T_m, yields Equation 5.6:

$$T_m = \frac{x_{Cu}\Delta H^f_{Cu} + x_{Sn}\Delta H^f_{Sn}}{x_{Cu}\Delta S^f_{Cu} + x_{Sn}\Delta S^f_{Sn} + x_{Cu}\ln x_{Cu} + x_{Sn}\ln x_{Sn}} \qquad (5.6)$$

Substituting the values of Table 5.1 into Equation 5.6 the hypothetical congruent melting temperature for the intermetallic Cu_6Sn_5 phase is found to be T_m = 951 K (678 °C). Therefore, to drive Cu diffusion through the intermetallic Cu_6Sn_5 layer at a sufficient rate, a casting temperature of 650 °C would seem to be most reasonable of the temperatures chosen in this study.

Table 5.1 Enthalpies and entropies of formation for Cu, Sn and Cu_6Sn_5.

Chemical Formula	ΔH^f, J/mol	ΔS^f, J/mol • K
Cu (59)	13100	9.6
Sn (60)	7300	13.9

When comparing the microstructure of the samples cast at 500 °C for 45 minutes and 15 hours very little difference was noticed. Both samples contained intermetallics (dark contrast) surrounded by a eutectic matrix and no undissolved Ag or Cu was observed (see Figures 4.7*b*, *c*). The sample cast at 500 °C for 16 hours was probably completely homogenized due to the long time which allowed for complete diffusion of the Cu into the liquid Sn. The slight differences between them are the relative amount of intermetallic phases present. This difference could perhaps be accounted for if the samples were cooled at slightly different rates. In the casting procedure used, the cooling rate was not stringently controlled and there was some minor cooling rate variation from sample to sample. Also, within a given sample the cooling rate may have varied since the sample was dipped into water with only one side initially coming into contact with the water. For common industrial practice, casting the alloy at 650 °C for 45 minutes would be sufficient to allow for complete homogenization and the generation of an optimum cast microstructure.

5.3. Cooling Rate Study

The microstructure of an as-cast solder joint is very dependent on cooling rate. This has important implications when considering parameters for an industrial soldering process. If the soldering process results in the joint being slowly cooled (0.1-1 °C/sec), then the solder's microstructure will be rather coarsened with large intermetallics present. This is almost never desired. With a faster cooling rate the solder will be stronger and have a more refined microstructure.

Another important aspect of knowing the solders microstructure is in mechanical testing. There have been many recent studies which deal with the strength and resistance to thermal-mechanical fatigue of Pb-bearing and Pb-free solders. If the results of such tests are to be meaningful the initial microstructure of the solders involved must be known and controlled. The most accurate and meaningful results can be obtained by solidifying the solder alloys in a consistent manner and one which corresponds to actual soldering processes.

The eutectic spacing of the Sn-4.7Ag-1.7Cu wt% solder samples cooled at different rates was examined using SEM. The eutectic microstructure present in these samples does not have a regular spacing which was measurable. From Figures 4.14*a-d* it can be seen that the eutectic microstructure appears to be composed of small intermetallics (light contrast) in a β-Sn matrix (dark contrast).

The cooling rate of the Sn-4.7Ag-1.7Cu wt% solder samples did have a noticeable effect on the formation of coarsened intermetallics. In the samples subjected to high cooling rates, the formation of intermetallics was limited to near the Cu-solder interface. While the molten solder was in contact with the Cu substrate it probably became richer in Cu near the interface. As a result, the local composition of the solder at the Cu-solder interface became

Cu rich which promoted the formation of Cu rich intermetallics in the solder upon solidification.

When cooled at slower rates, the solder's microstructure contained coarsened intermetallics surrounded by what appears to be a eutectic matrix. The coarsened intermetallic formation during solidification appears to have a kinetic dependence. The stability of the eutectic interface during solidification is possibly dependent on the relative growth rates of the intermetallic phases (Ag_3Sn and Cu_6Sn_5) and the β-Sn phase. The stability of the growth front could also be affected by a faceted/non-faceted growth front composed of the three competing phases. Cu_6Sn_5, with its hexagonal close packed structure, has a faceted growth front while β-Sn has a non-faceted growth front. For a faceted/non-faceted eutectic growth front, the coupled growth zone below the eutectic plane can be skewed towards the faceted phase (61). This could result in an alloy of eutectic composition exhibiting dendritic growth of the non-faceted phase if undercooling is sufficient enough. Such an effect would be accentuated if the selected alloy composition is slightly off eutectic towards the faceted intermetallic phases.

The undercooling of the samples used in this cooling rate study was unknown due to lack of sensitivity in thermocouple placement but is probably not significant due to the liquid solder's intimate contact with the rough, polycrystalline Cu substrate surface. It was assumed that the undercooling for each sample was essentially the same since the factors assisting nucleation were basically constant. Each sample was solidified on a Cu block and the heat flow was through the Cu block away from the Cu-solder interface. Therefore, nucleation most likely occurred at the Cu/solder interface and the growth front moved away from this interface into the solder bulk.

The coarsened intermetallics present in the microstructure most likely did not develop behind the solid/liquid growth interface (i.e., via diffusion in the newly formed solid) since Sn-4.7Ag-1.7Cu wt% solder samples which were annealed at 170 °C for 5000 seconds showed little to no coarsening (see Table 4.5). The diffusivity of the Sn, Ag and Cu atoms is simply too low for any significant intermetallic coarsening in the solid to occur at the times and temperatures used in the cooling rate experiments. This implies that a cooperative eutectic growth solid/liquid interface is unstable at slow cooling rates and that the individual phases grow in a divorced fashion out of the liquid. It is possible that the intermetallic phases shoot out ahead of the β-Sn phase at slow cooling rates. This would account for the large coarsened intermetallics seen in Figures 4.13*a*,*b*. An effective method for additional study of the solid/liquid interface morphology of the Sn-4.7Ag-1.7Cu wt% solder would be to directionally solidify the solder over a range of growth rates. This would probably reveal what mechanism is responsible for the instability of the eutectic growth front.

At the Cu/solder interface an intermetallic layer of Cu_6Sn_5 forms, as can be seen in Figure 4.9. This layer also formed at the Cu/solder interface of the cooling rate experiment samples. It can be hypothesized that some intermetallic particles break free of the interface and coarsen in the liquid solder and this mechanism is responsible for the coarsened intermetallics seen in samples which were slowly cooled. However, this sort of coarsening mechanism is highly unlikely under the conditions used in this experiment. The liquid solder was in contact with the Cu block for no longer than 300 seconds (slow cooled case) at a temperature lower than 250 °C. In Figure 4.7*a* it can be seen that even when Cu is in liquid Sn at 300 °C for 45 minutes no coarsened Cu_6Sn_5 intermetallics form because of a deficiency of dissolved Cu. As discussed in Section 5.2, this is due to the formation of an intermetallic layer at the Cu/liquid solder interface. Therefore, only trace amounts of Cu could diffuse through the intermetallic layer into the solder while the solder was in contact with the Cu block at 250 °C for 300 sec. It is suggested that a future experiment be constructed where the time at which the molten solder is on the Cu block is varied as well as cooling rate and the resulting microstructure examined for the size of coarsened intermetallics.

Even though not explicitly visible, the eutectic microstructure of the Sn-4.7Ag-1.7Cu wt% solder does most probably solidify with a finer spacing at higher cooling rates. This would explain the pronounced increase in hardness corresponding to increase in cooling rate (see Figure 4.15). It is well known that finer eutectic microstructures are more resistant to deformation than coarsened eutectic microstructures. The increase in hardness can also be correlated with an increase in strength in the solder, although this was not studied. This is important for circuit board assembly manufacturers. To achieve a microstructure of optimum strength the fastest cooling rate possible is desired.

The hardness of the through hole solder joints were compared with the hardness of the microstructure stability study samples. The joints annealed at 130 °C for 1000 seconds had a Vickers DP hardness of about 25 which corresponds to a cooling rate of 1-10 °C/sec (see Figure 4.10). The microstructures of these samples are also similar. These results demonstrate that for a given Sn-4.7Ag-1.7Cu wt% sample, hardness can be correlated to a real solder joint's cooling rate and microstructure.

5.4. Microstructural Stability

An important aspect of any solder used in today's demanding microelectronic applications is the stability of the microstructure when subjected to severe environments, i.e., thermal cycling, fatigue, etc. Therefore, the stability of the Sn-4.7Ag-1.7Cu wt% solder's microstructure when annealed at relatively high homologous temperatures for different periods of time was investigated.

It was found that the intermetallics present in the solder coarsened at high annealing temperatures for long times. The coarsening, however, led to a more rounded morphology of the intermetallics and an increase in particle aspect ratio. The increase in the average intermetallic particle size was expected. The rounded morphology of the coarsened intermetallics is advantageous with respect to strength. Crack initiation which leads to failure often starts at areas within the microstructure with the highest stress concentrations. Rounded particles have a lower stress concentration than particles which are needle like.

The coarsening of the intermetallic particles was not significant at the annealing temperature of 130 °C. This result is important when considering automotive applications because under the hood environments are not likely to exceed 150 °C. Coarsening is a diffusion controlled process. The diffusivity of Cu and Ag in Sn at this temperature is too low for any significant coarsening to occur, except when held at temperature for long periods of time, especially when both solute elements are closely bound in intermetallic phases. The length of time of the anneal was a factor in the evolution of the area percent of the intermetallics. Long times at all temperatures resulted in an increase in both average particle size and average particle area. A full kinetic analysis of the coarsening and multiphase diffusion phenomenon, however, is beyond the scope of this work but could prove worthwhile as a future study.

6. CONCLUSIONS

A new Pb-free solder, Sn-4.7Ag-1.7Cu wt%, has been developed which shows great promise as a Pb-free solder system. This solder exhibits a ternary eutectic reaction, i.e., contains a class I four-phase equilibrium, $L \Rightarrow \eta + \theta + \beta$-Sn ($\eta$ = Cu_6Sn_5, θ = Ag_3Sn) at a temperature of 217 ± 0.5 °C. Initial trial solder joints made with this solder revealed that the Sn-4.7Ag-1.7Cu (wt%) alloy can function as a solder by wetting and forming a high quality bond with copper. The melting temperature of 217 °C is slightly higher than currently available Sn-Pb solder pastes (T_{eut} = 183 °C). With further modifications, such as quaternary alloying additions based on experimental and theoretical phase diagram relationships, the properties of the Sn-Ag-Cu solder may be enhanced to provide an alternative solder alloy for many conventional leaded solders used in electronic applications.

Using DTA it was determined that a ternary eutectic reaction does exist in the Sn rich region. Solidus and liquidus temperatures observed from DTA proved sufficient in mapping out isopleth sections in the Sn-rich corner of the Sn-Ag-Cu phase diagram. However, it is suggested that phase diagram studies of this system in the future employ directional solidification as a supplement to such a study. In addition, isopleth sections which do not involve complications, such as liquidus trough intersection, would provide additional useful data.

The Sn-4.7Ag-1.7Cu wt% solder alloy shows potential as a replacement solder in situations where operating conditions are severe, i.e., automotive, aerospace etc. The microstructural stability of the alloy, retaining 60% original hardness (i.e., strength) even after annealing for 10^6 seconds at a homologous temperature of 0.98, indicates acceptable performance. In addition to retained hardness, the rounded morphology of the coarsened microstructure is more likely to discourage crack initiation during thermal-mechanical fatigue.

The solder's as-cast microstructure is dependent on the cooling rate employed during solidification. At cooling rates less than about 1 °C/sec (corresponding to slow reflow cooling), the intermetallic phases of the eutectic microstructure coarsen and grow separate from the eutectic. At cooling rates greater than about 10 °C/sec (corresponding to hand soldered joints) the solder's microstructure is composed almost entirely of a finely spaced eutectic. This microstructure was the strongest of those found in this work. When performing mechanical tests on the Sn-4.7Ag-1.7Cu wt% and other solders it is important to know and control the cooling rate. Without a meaningful (i.e., similar to real world practices in the microelectronic industry) and consistent microstructure as a reference from sample to sample, mechanical tests are dubious.

Parameters in casting the solder such as temperature and the time at temperature are important in assuring that each higher melting (Ag and Cu) elemental constituent becomes dissolved. It was found that casting the Sn-4.7Ag-1.7Cu wt% alloy at 650 °C for 45 minutes proved sufficient for complete melting and should serve well for actual bulk casting processes.

REFERENCES

1. D. R. Frear, M. M. Rashid, S. N. Burchett, *Microstructurally Based Thermomechanical Fatigue Lifetime Model of Solder Joints for Electronic Applications*, Procedings from ASME Design Technical Conference (ASME, Albuquerque, NM, 1993).

2. P. T. Vianco, D. R. Frear, *JOM* **45**, July (1993): 14-19.

3. M. Whitmore, *Soldering and Surface Mount Technology* **15**, October (1993): 2.

4. C. Lüchinger, J. Beuers, A. Fiebig, W. Werner, *Advanced Packaging* , Jan/Feb (1994): 14.

5. J. S. Hwang, G. Lucey, R. B. Clough, J. Marshall, *Surface Mount Technology* , September (1991): 40-41.

6. H. H. Manko, *Solders and Soldering: Materials, Design Production and Analysis for Reliable Bonding* (McGraw-Hill, Inc., New York, 1992).

7. R. J. K. Wassink, *Journal of the Institute of Metals* **95**, (1967): 38-43.

8. F. G. Yost, Personal Communication, 1993.

9. A. J. Sunwoo, H. Hayashigatani, J. J. W. Morris, J. G. K. Lucey, *JOM* **43**, June (1991): 21-24.

10. R. J. K. Wassink, *Soldering in Electronics* (Electrochemical Publications Limited, Ayr, Scotland, 1984).

11. L. P. Lambert, *Soldering for Electronic Assemblies*. G. Boothroyd, G. E. Dieter, Eds., Manufacturing Engineering and Materials Processing (Marcel Dekker, Inc., New York, New York, 1988), vol. 25.

12. J. H. Lau, *Solder Joint Reliability: Theory and Applications* (Van Nostrand Reinhold, New York, 1991).

13. C. C. Johnson, J. Kevra, *Solder Paste Technology: Principles and Applications* (Tab Professional and Reference Books, Blue Ridge Summit, PA, 1989).

14. P. G. Harris, M. A. Whitmore, *Circuit World* **19**, Jan (1993): 25-27.

15. W. L. Winterbottom, *JOM* **45**, July (1993): 20-24.

16. February 1993 prices from Kester, Gardiner and ESP for same paste (-200+325 mesh, 85 vol% powder, 550 kcps, water soluable flux).

17. F. G. Yost, *Pb-Free Soldering Technology*, Pollution Prevention Technologies: Industry Exchange Workshop San Antonio, TX, 1993), pp. 19.

18. U. S. Congress, House, 1993 (H-2479).

19. D. Swanson, *Electronic Packaging and Production* , December (1991): 7.

20. "What Else is in the Refrigerator?", *Consumer Reports*, 1994, Feb., pp. 100.

21. U. S. Congress, Senate, 1990 (S-2637).

22. D. L. Simms, *The Science of the Total Environment* **71**, 3 (1988): 487-491.

23. World Health Organization, *Environmental Health Criteria 3: Lead*, vol. 3 (World Health Organization, Geneva, 1977).

24. A. Cory-Slechta, *The Science of the Total Environment* **71**, 3 (1988): 433-440.

25. J. M. Ratcliffe, *Lead in Man and the Environment* (Ellis Horwood Limited, New York, 1981).

26. S. R. Schroeder, Eds., *Toxic Substances and Mental Retardation*, vol. 8 (American Association on Mental Deficiency, Washington D. C., 1987).

27. J. O. Nriagu, Eds., *Topics in Environmental Health: The Biogeochemistry of Lead in the Environment, Part B. Biological Effects*, vol. (Elsevier/North-Holland Biomedical Press, Amsterdam, Netherlands, 1978).

28. J. L. Annest, *Trends in the Blood Lead Levels of the US Population*, M. Rutter, R. R. Joness, Eds., International Symposium on Low Level Lead Exposure and Its Effects on Human Beings (John Wiley & Sons, London, England, 1982), pp. 33-58.

29. H. L. Needleman, *Low Level Lead Exposure and Neurophychological Performance*, M. Rutter, R. R. Joness, Eds., International Symposium on Low Level Lead Exposure and Its Effects on Human Beings (John Wiley & Sons, London, England, 1982), pp. 229-248.

30. G. Winneke, *Neurobehavioural and Neuropsychological Effects of Lead*, M. Rutter, R. R. Joness, Eds., International Symposium on Low Level Lead Exposure and Its Effects on Human Beings (John Wiley & Sons, London, England, 1982), pp. 249-265.

31. M. Rutter, *Low Level Lead Exposure: Sources, Effects and Implications*, M. Rutter, R. R. Joness, Eds., International Symposium on Low Level Lead Exposure and Its Effects on Human Beings (John Wiley & Sons, London, England, 1982), pp. 333-370.

32. R. Lansdown, W. Yule, Eds., *The Lead Debate: The Environment, Toxicology and Child Health*, vol. (Croom Helm, London, England, 1986).

33. S. Binder, H. Falk, *Strategic Plan for the Elimination of Childhood Lead Poisoning* (U. S. Department of Health and Human Services, Wahington D. C., 1991).

34. W. L. Roper, *Preventing Lead Poisoning in Young Children* (U. S. Department of Health and Human Services, Washington D. C., 1991).

35. U. S. Congress, House, 1991 (H-2922).

36. K. Bae, A. F. Sprecher, H. Conrad, D. Y. Young, *Fatigue of 63Sn-37Pb Solder Used in Electronic Packaging*, ISTFA 1988: International Symposium for Testing and Failure Analysis: The Failure Analysis Forum for Microelectronics and Advanced Materials. (ASM International, Los Angeles Airport Marriott Hotel, Los Angeles, CA, USA, 1988), pp. 53-61.

37. D. R. Frear, P. T. Vianco, *Metallurgical Transactions* , (1993): 110-125.

38. D. R. Frear, *IEEE Transactions on Components, Hybrids, and Manufacturing Technology* **12**, 4 (1989): 492-501.

39. C. Melton, *Alternatives of Lead Bearing Solder Alloys*, IEEE International Symposium on Electronics and the Environment (IEEE, Arlington, VA, USA, 1993), pp. 94-97.

40. D. Frear, D. Grivas, J. W. M. Jr., *Journal of Electronic Materials* **16**, 3 (1987): 181-186.

41. M. McCormack, S. Jin, *JOM* **45**, July (1993): 36-40.

42. M. McCormack, S. Jin, H. S. Chen, D. A. Machusak, *Journal of Electronic Materials* **23**, July (1994): 687-690.

43. M. McCormack, S. Jin, *Journal of Electronic Materials* **23**, July (1994): 635-640.

44. E. Gebhardt, G. Petzow, *Zeitschrift für Metallkunde* **50**, 10 (1959): 597-605.

45. M. E. Brown, *Introduction to Thermal Analysis Techniques and Applications* (Chapman and Hall, Cambridge, 1988).

46. W. W. Wendlandt, *Thermal Methods of Analysis*. P. J. Elving, I. M. Kolthoff, Eds., Checical Analysis (Interscience Publishers, New York, 1964), vol. 19.

47. F. E. Wang, F. A. Kanda, A. J. King, *Journal of Physical Chemistry* **66**, Nov (1962): 2138-2142.

48. W. J. Smothers, Y. Chiang, *Handbook of Differential Thermal Analysis* (Chemical Publishing Company, Inc., New York, 1966).

49. M. B. Panish, *Journal of Physical Chemistry of Solids* **27**, (1966): 291-298.

50. N. A. Nedumov, in *Differential Thermal Analysis: Fundamental Aspects* R. C. Mackenzie, Eds. (Academic Press, London, 1970), vol. 1, pp. 161-191.

51. T. Heumann, O. Alpaut, *Journal of the Less-Common Metals* **6**, (1964): 108-117.

52. W. F. Hemminger, H. K. Cammenga, *Methoden der Thermischen Analyse*. W. Fresenius, J. F. K. Huber, E. Pungor, G. A. Rechnitz, W. Simon, G. Tölg, T. S. West, Eds., Anleitungen für die chemische Laboratoriumspraxis (Springer-Verlag, Berlin, 1989), vol. 24.

53. W. Gutt, A. J. Majumdar, in *Differential Thermal Analysis: Applications* R. C. Mackenzie, Eds. (Academic Press, London, 1972), vol. 2, pp. 79-117.

54. T. Daniels, *Thermal Analysis* (Halsted Press, Great Britain, 1973).

55. I. E. Anderson, Master of Science Thesis, University of Wisconsin-Madison (1977).

56. F. N. Rhines, *Phase Diagrams in Metallurgy: Their Development and Application*. R. F. Mehl, M. B. Bever, Eds., Metallurgy and Metallurgical Engineering Series (McGraw-Hill, New York, 1956).

57. C. M. Miller, I. E. Anderson, J. F. Smith, *Journal of Electronic Materials* **23**, 7 (1994): 595-601.

58. D. R. Lide, Eds., *CRC Handbook of Chemistry and Physics*, vol. (CRC Press, Boston, 1990).

59. R. Hultgren, P. D. Desai, D. T. Hawkins, M. Gleiser, K. K. Kelley, *Selected Values of the Thermodynamic Properties of Binary Alloys* (American Society of Metals, Metals Park, OH, 1973).

60. R. Hultgren, P. D. Desai, D. T. Hawkins, M. Gleiser, K. K. Kelley, D. D. Wagman, *Selected Values of the Thermodynamic Properties of the Elements* (American Society for Metals, Metals Park, OH, 1973).

61. W. Kurz, D. J. Fisher, *Fundamentals of Solidification* (Trans Tech Publications Ltd., Netherlands, 1992).

ACKNOWLEDGMENTS

I would first like to acknowledge Nile Beymer for showing me that it doesn't take a college degree to become as wise as those with college degrees, but that with hard work, dedication and experience, true wisdom can be obtained.

For assistance in experimental work I would like to acknowledge Jack F. Smith for valuable advice and help with this project, Hal Sailsbury for metallography work, Kevin Dennis for DTA maintenance, Dr. Leonard S. Chumbley for excellent SEM training and fine housing, Fran Laabs for SEM sample preparation, Alfred Kracher for superb WDS work and my office mates Matt Osborne, Joel Flumerfelt and Jeff Moore for their wisdom on various things. Dr. Kayser and Dr. Verhoeven also are due credit for sparking my interest in metallurgy. I would like to thank Iver Anderson for giving me the chance to work with a practical research project and understanding that projects get behind schedule once in a while. :)

I would especially like to thank the Red Frog, who so faithfully got me to work nearly every day. The Frog also gave stellar performances on the weekly 500 mile trips from Ames to Davenport and back. "All too easy," I once heard him say... 2.39 x10^5 miles of Frog Patrol, and still going strong on the quest for 2.50 x 10^5. The ISU Parking Systems and Gilman hall construction crews also deserve some credit for allowing Froggy to rest his weary crank shaft right outside Gilman most every day all semester long without a ticket.

I would also like to acknowledge the financial support provided by the United States Department of Energy under the Office of Energy Research and the Environmental Restoration and Waste Management Office. This work was performed at Ames Laboratory under Contract No. W07405-eng-82 and TTP no. CH133001 with the U. S. Department of Energy. The United States government has assigned the DOE Report number IS T1-1728 to this thesis.

APPENDIX: DTA CURVES

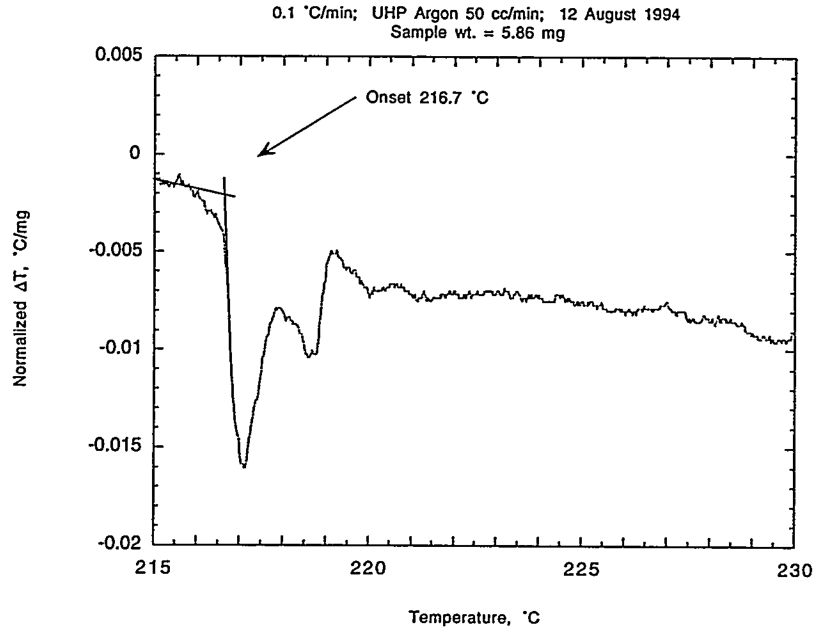

a)

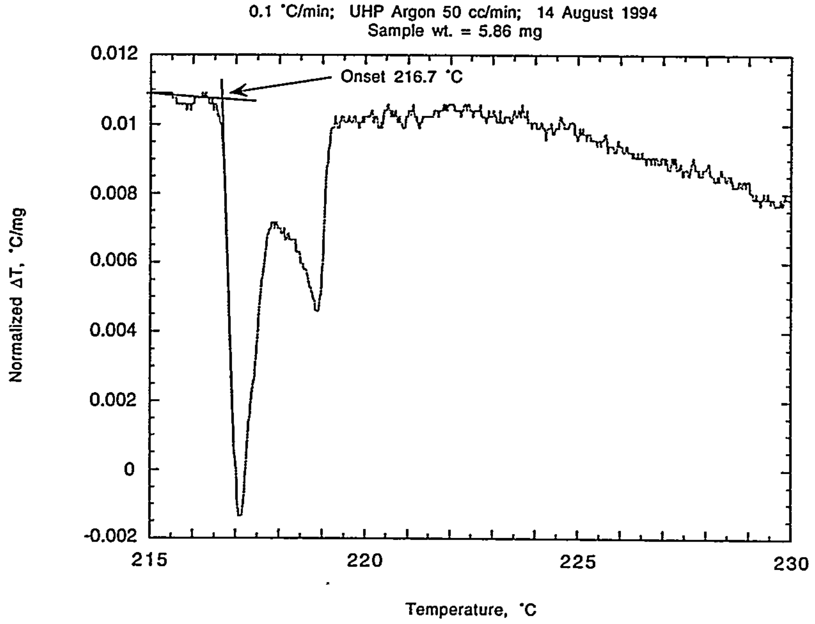

b)

***Figure* A1** DTA thermograms of the Sn-3.8Ag-0.4Cu wt% sample (PDM1).

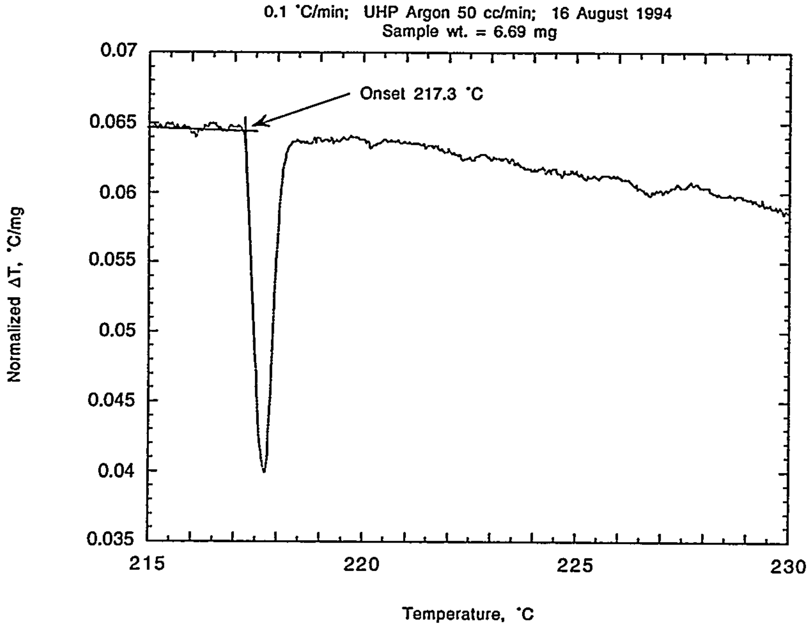

a)

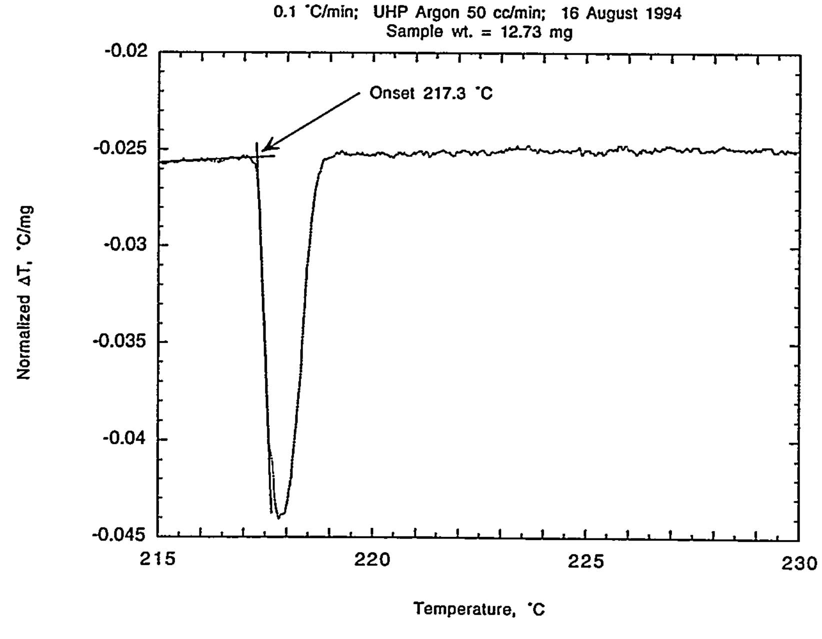

b)

***Figure* A2** DTA thermograms of the Sn-4.1Ag-0.9Cu wt% sample (PDM2).

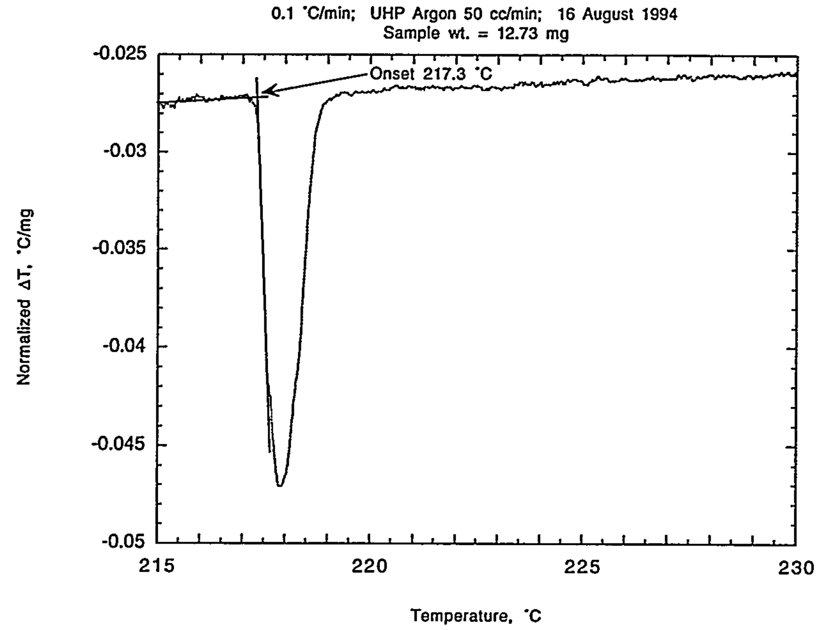

***Figure* A3** DTA thermograms of the Sn-4.4Ag-1.3Cu wt% sample (PDM3).

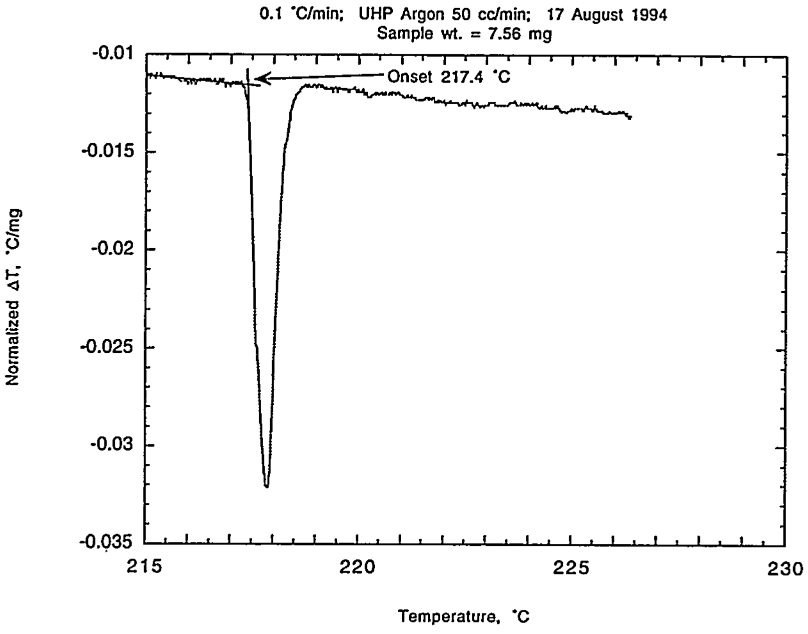

a)

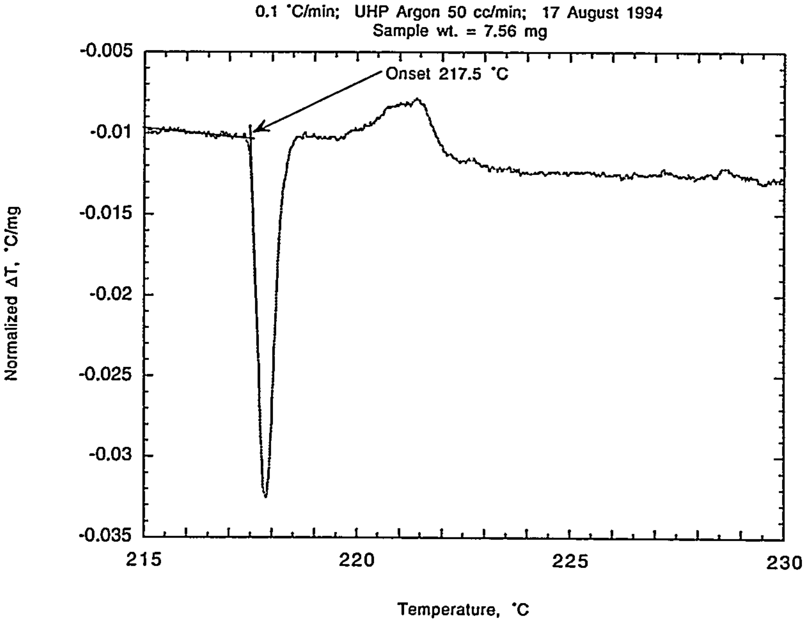

b)

***Figure* A4** DTA thermograms of the Sn-5.0Ag-2.1Cu wt% sample (PDM4).

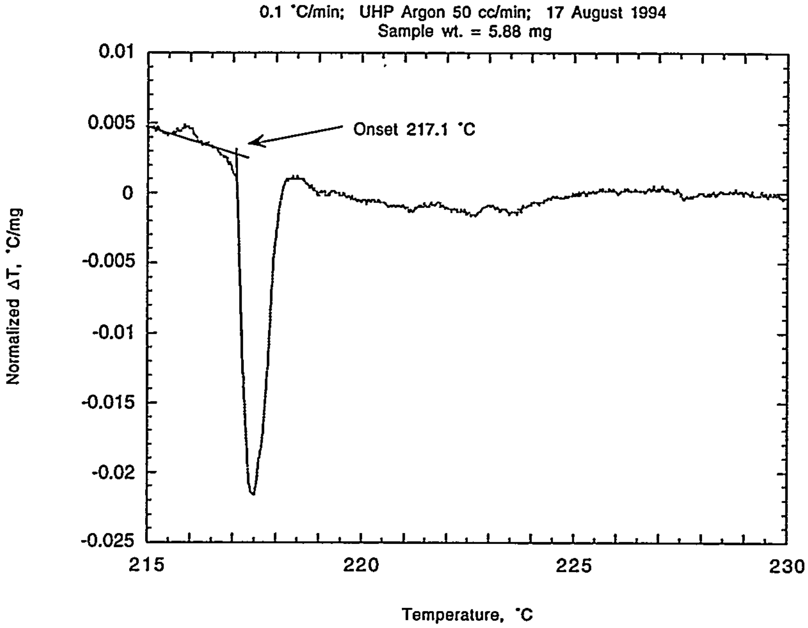

a)

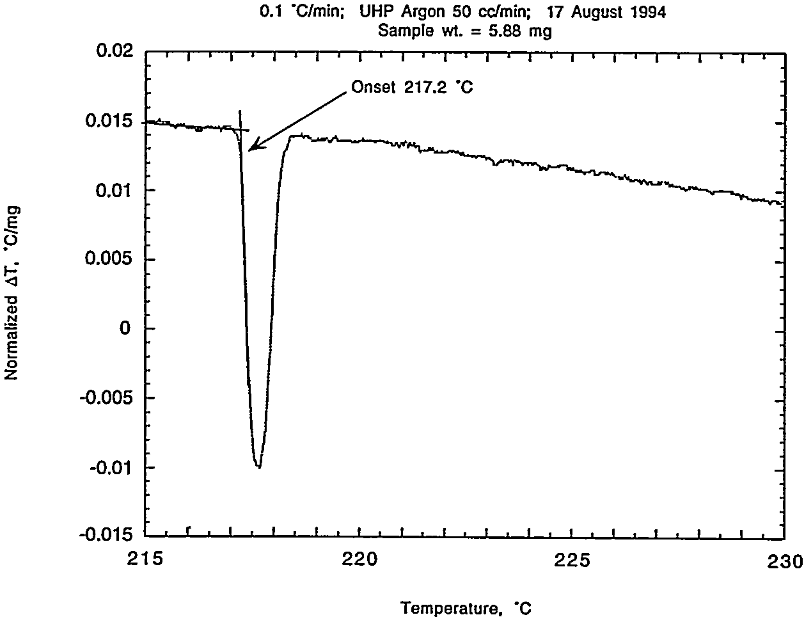

b)

***Figure* A5** DTA thermograms of the Sn-5.5Ag-2.8Cu wt% sample (PDM5).

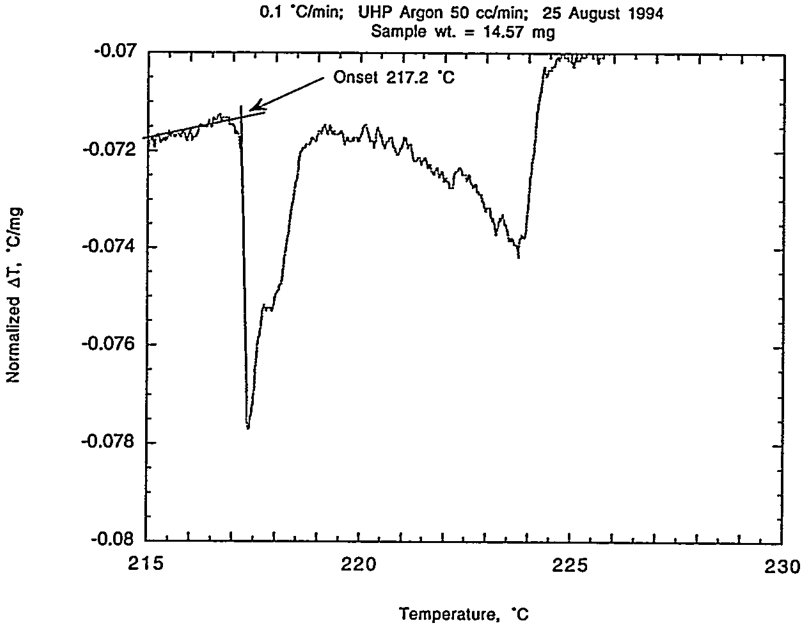

a)

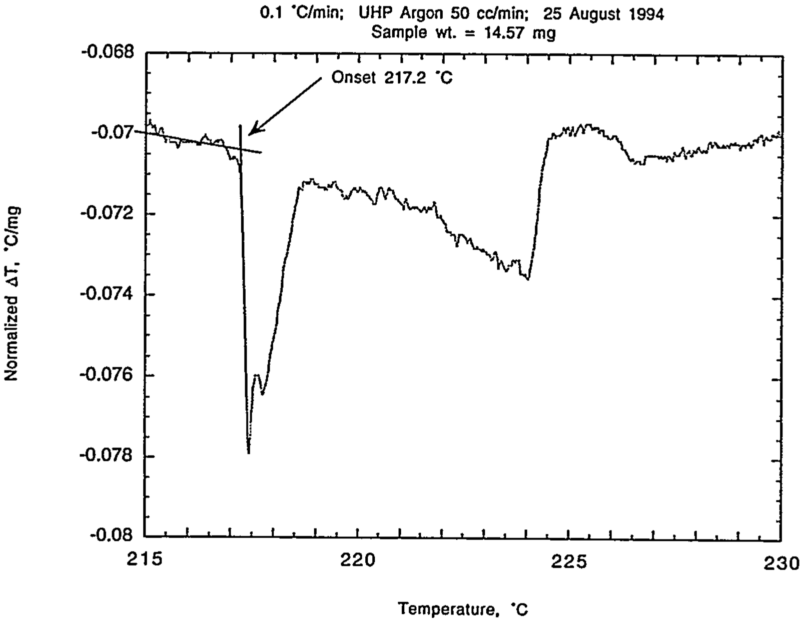

b)

***Figure* A6** DTA thermograms of the Sn-1.1Ag-1.1Cu wt% sample (PDM6).

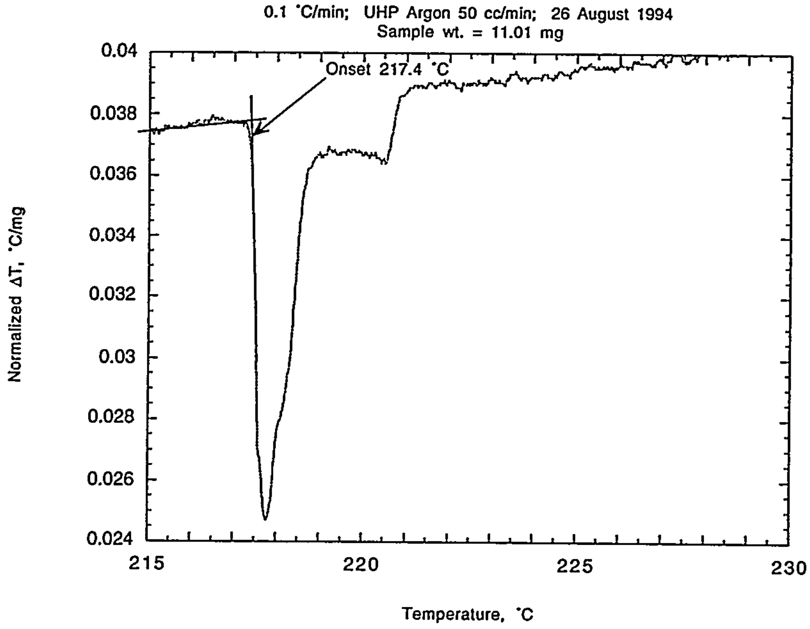

a)

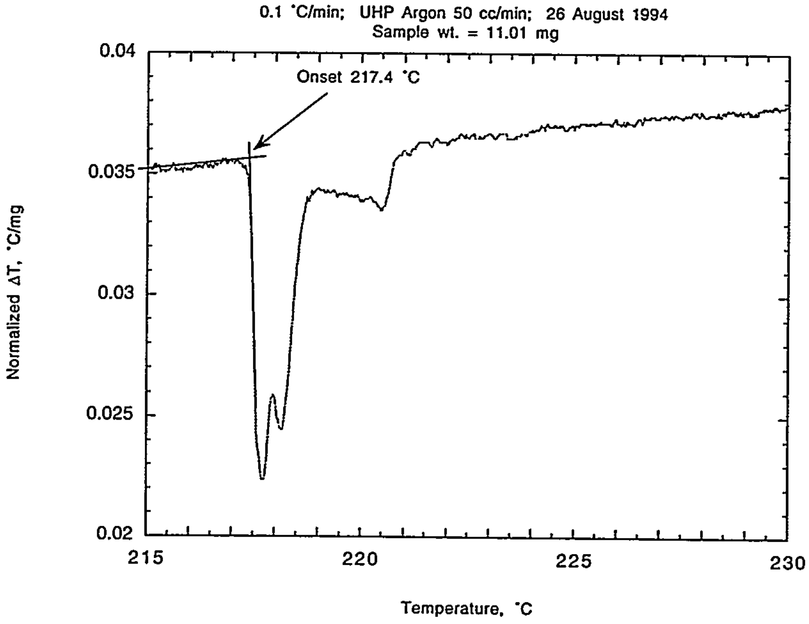

b)

***Figure* A7** DTA thermograms of the Sn-2.3Ag-1.3Cu wt% sample (PDM7).

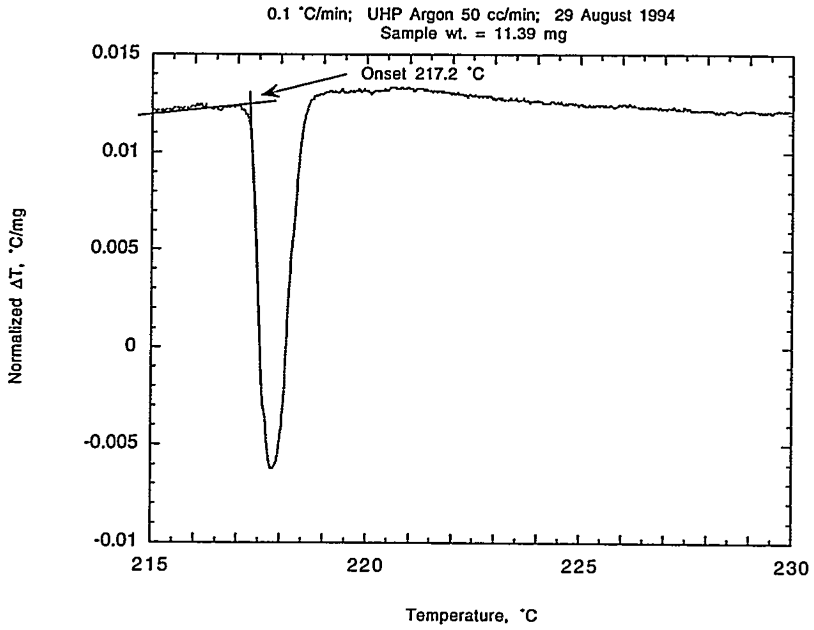

a)

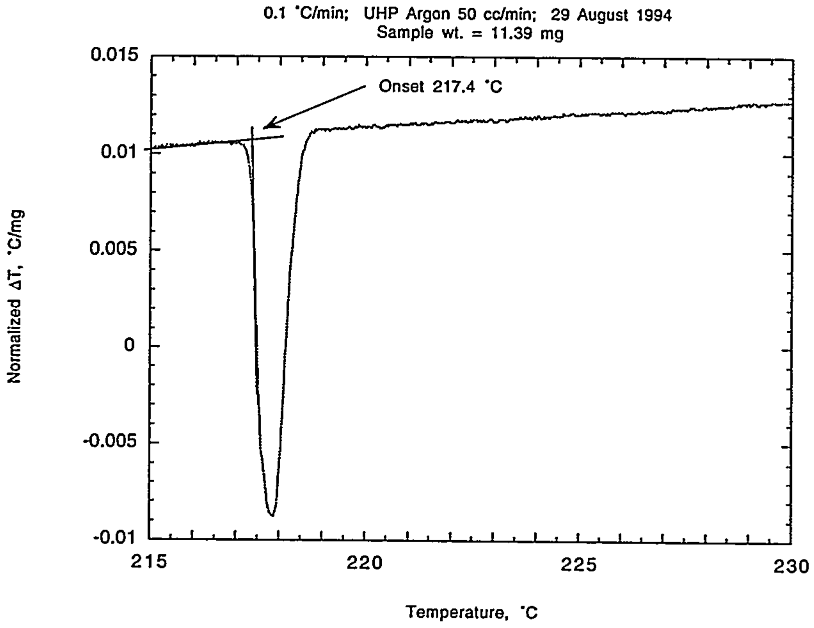

b)

***Figure* A8** DTA thermograms of the Sn-3.6Ag-1.5Cu wt% sample (PDM8).

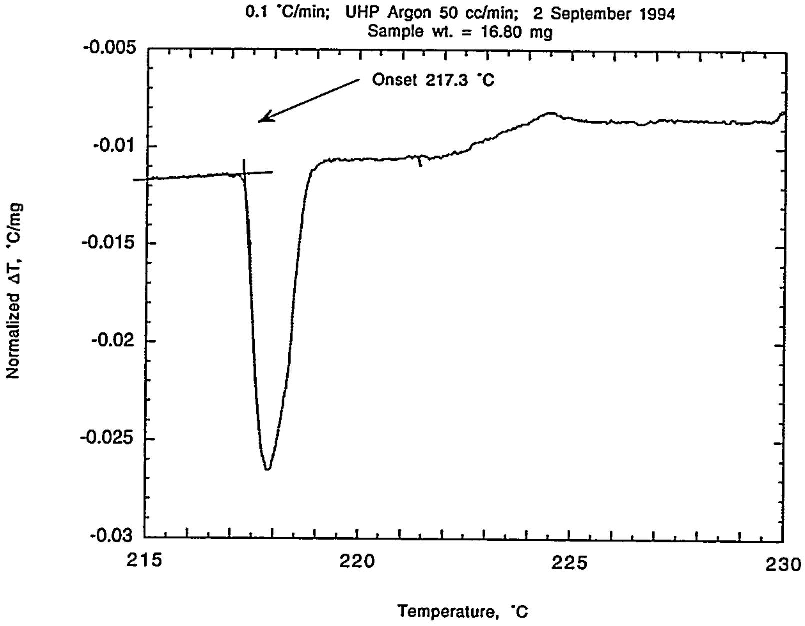

a)

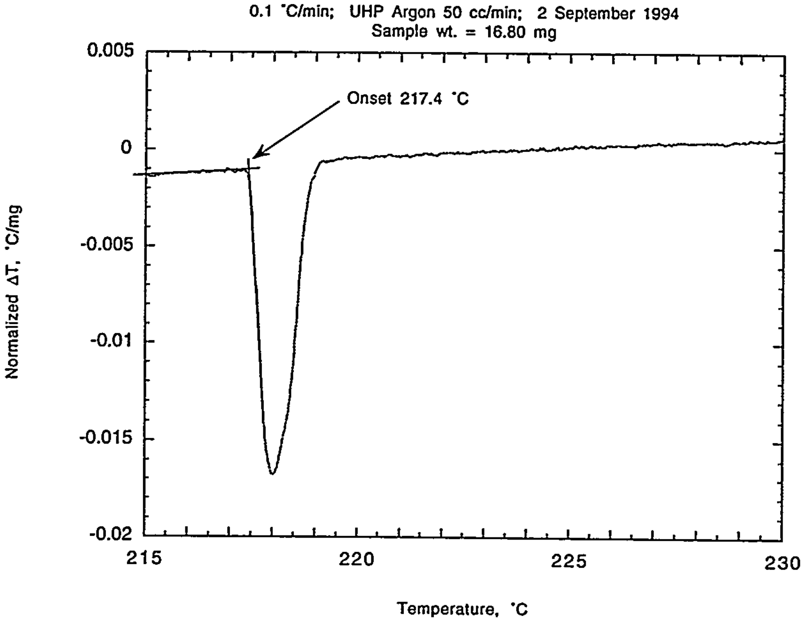

b)

***Figure* A9** DTA thermograms of the Sn-6.1Ag-1.9Cu wt% sample (PDM9).

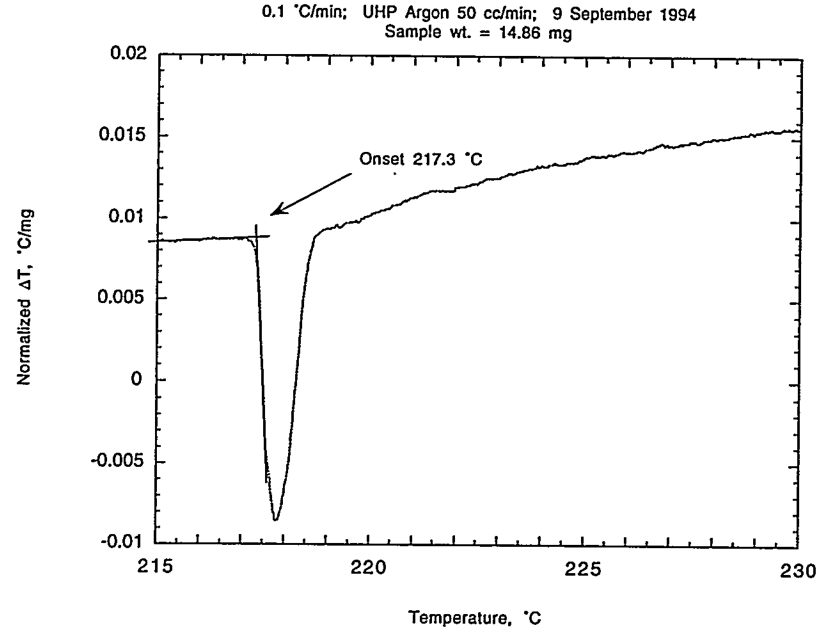

a)

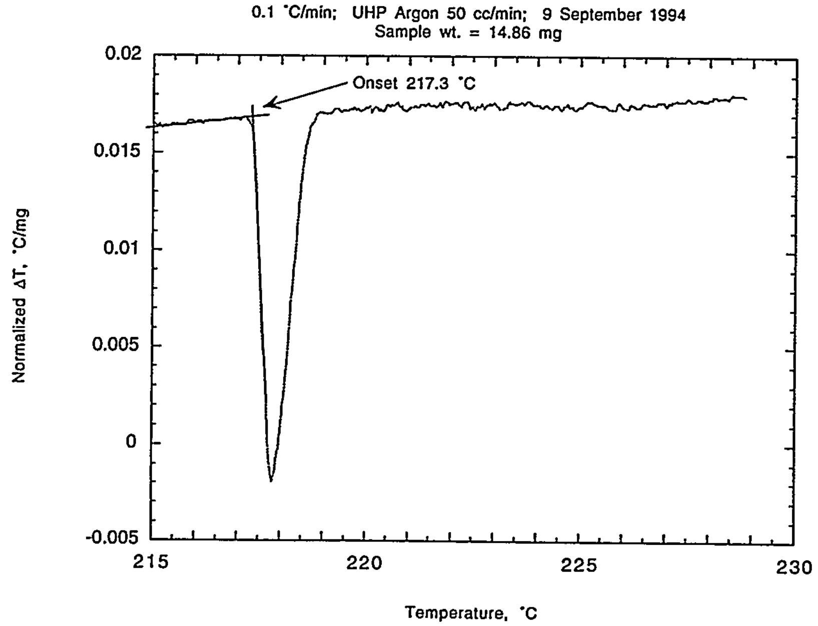

b)

***Figure* A10** DTA thermograms of the Sn-7.4Ag-2.1Cu wt% sample (PDM10).

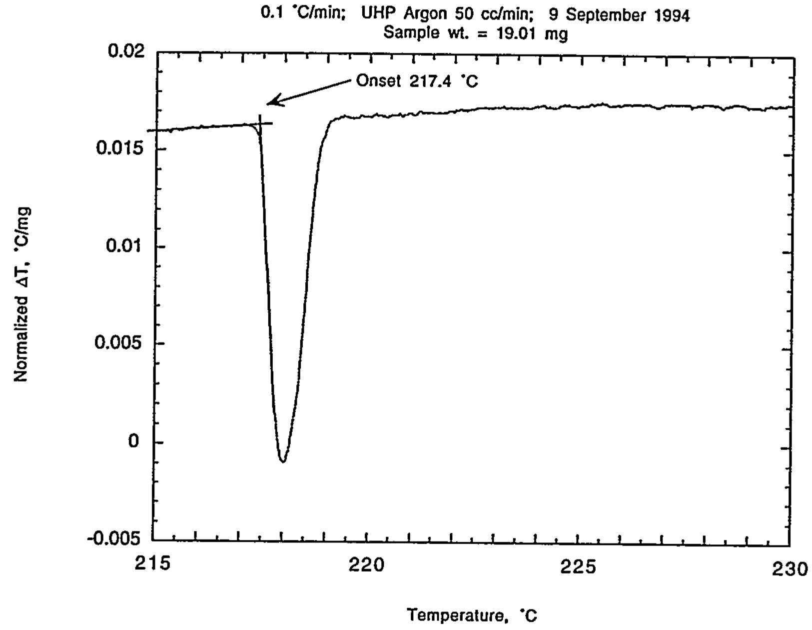

a)

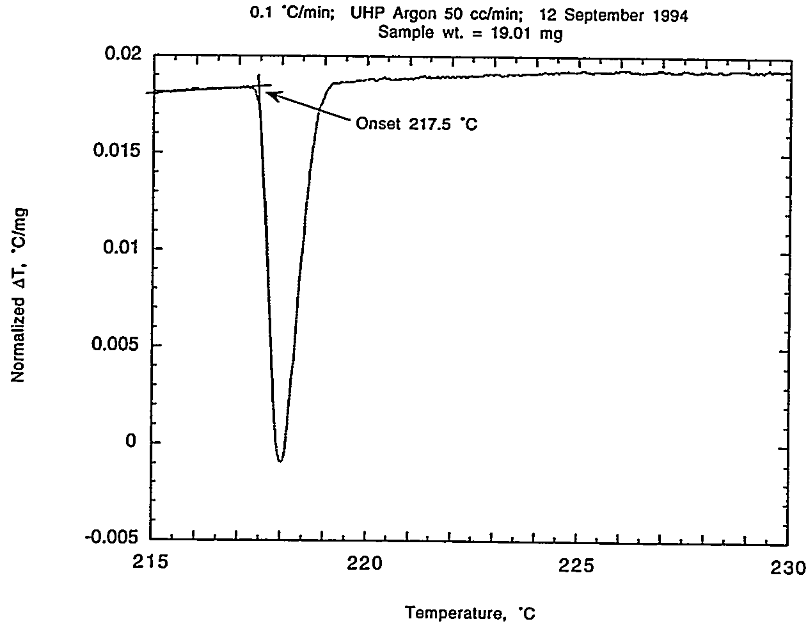

b)

***Figure* A11** DTA thermograms of the Sn-4.7Ag-1.7Cu wt% sample (PDM11).

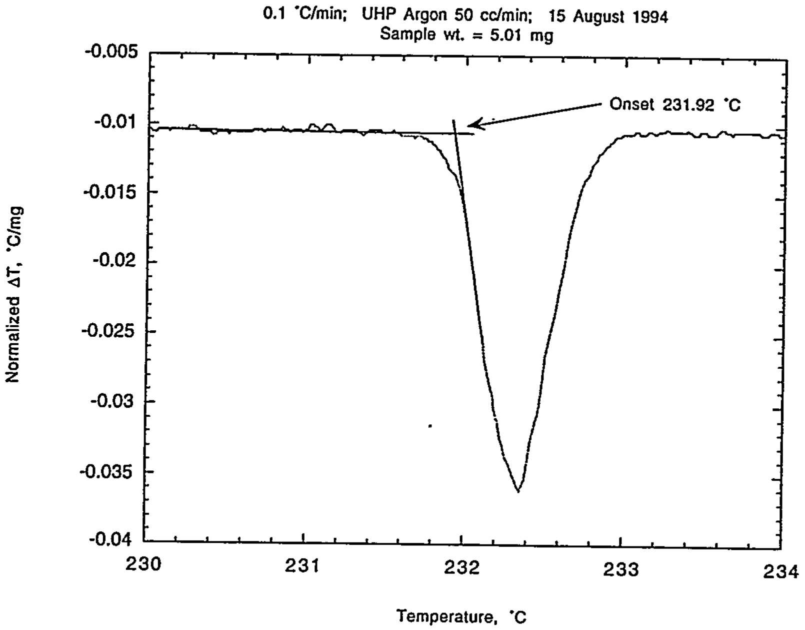

***Figure* A12** DTA thermogram of pure Sn (99.99%), from an emulsified powder sample.